

REPORT DOCUMENTATION PAGE

FORM APPROVED
OMB No. 0704-0188

Public reporting burden for this collection of information is estimated to average 1 hour per response, including the time for reviewing instructions, searching existing data sources, gathering and maintaining the data needed and completing and reviewing the collection of information. Send comments regarding this burden estimate or any other aspect of the collection of information, including suggestions for reducing the burden to Washington Headquarters Services, Directorate for Information Operations and Reports, 1215 Jefferson Davis Highway, Suite 1204, Arlington, VA 22202-4302 and to the Office of Management and Budget, Paperwork Reduction Project (0704-0188), Washington, DC 20503

ONBCHI COMPUTER V 1.0 11/94

DTIC QUALITY INSPECTED A

STANDARD FORM 298 (REV 2-89)

FINAL REPORT

on

**SUPERSONIC MIXING ENHANCEMENT
USING PULSED TRANSVERSE FUEL JETS**

by

Ahmad D. Vakili, Y.K. Chang and J.M. Wu
The University of Tennessee Space Institute
Tullahoma, Tennessee 37388

for

ONR Grant Navy N0014-89-J-1696

19950911/062

August 1995

DTIC QUALITY INSPECTED 5

FINAL REPORT

on

**SUPERSONIC MIXING ENHANCEMENT
USING PULSED TRANSVERSE FUEL JETS**

by

Ahmad D. Vakili, Y.K. Chang and J.M. Wu
The University of Tennessee Space Institute
Tullahoma, Tennessee 37388

for

ONR Grant Navy N0014-89-J-1696

August 1995

Abstract

Pulsed jets have been shown to penetrate into a cross flow more than a corresponding steady state jet. The increased penetration depends to some extent on the formation of distinct ring vortices which in turn transport themselves into the cross-flow by the self induced velocity. This work has been concentrated in understanding the physics of the increased penetration. Experiments have indicated the formation of vortex rings as a jet was pulsed even when the propane fuel was combusting. The dynamics and trajectories of vortex rings formed by pulsation of a jet in a uniform cross-flow were studied and detailed measurements were made using flow visualization techniques including laser induced fluorescence and hot-film anemometry. Measurements indicated that vortex rings were fully-formed at a distance of three times the jet exit diameter. A numerical experiment based on a Lagrangian, grid-free, three-dimensional vortex method was performed and general agreement with the experiments was concluded. At low frequencies, interaction between adjacent vortex rings was negligible because of relatively large separation distances and under these conditions, each ring behaves like a single discrete vortex ring. It was observed that single vortex rings moved into the flow sometimes tilted up to about 30°, depending on the ring's strength. Tilting into the flow further contributed to the increased penetration. Numerical simulation showed that the tilting is due to the combined effect of viscosity and the cross-flow. Single pulses into a supersonic cross-flow also indicated the formation of vortex rings. Difficulties were experienced in accomplishing continuous pulsed injection into a supersonic cross-flow.

Table of Contents

1. Introduction	1
2. Experimental Procedures	4
2.1 Description of the Water Tunnel Facility	4
2.2 Experimental Setup for Continuous Pulsation	4
2.3 Hot-Film Anemometry and Data Acquisition	5
2.4 Flow Visualization Techniques	6
2.5 Measurement Uncertainties	7
3. Experimental Results	8
3.1 Motion of Vortex Rings in Crossflow	8
3.2 Tilting Mechanism for a Vortex Ring in Crossflow	9
3.3 Quantitative Measurements	10
3.4 Measurement of a Fully-Formed Vortex Ring	15
3.5 Dimensional Analysis for Pulsating Jet Trajectories	16
3.6 Blooming Rings	17
4. Combustion of Pulsed Fuel Jets	19
5. Numerical Study	22
5.1 Formulation and Numerical Scheme	23
5.2 Calculation Procedures	26
5.3 Simulation of Jet Source Flow	27
5.4 Numerical Results	29
6. Conclusions	32
Acknowledgements	33
References	34

List of Figures and Tables

Figures

1. Experimental setup of water tunnel for continuous pulsation	3
2. Typical pulsation profiles at the exit	3
3. Schematic diagram for thermal anemometer and data acquisition system	4
4. Typical photographs of vortex rings in cross-flow for various pulsation and flow conditions for $\bar{U}_j/U\infty = 1.5$, $Re_d = 1870$	
(a) Pulsed at 1 Hz, (b) Pulsed at 2 Hz, (c) Pulsed at 10 Hz, (d) Steady Jet,	
(e) Top view of a ring, jet is pulsed at 1 Hz.	
(f) A single ring moving into the cross-flow, note the upstream motion caused by the tilting process	5
5. Penetration trajectories of vortex rings in the cross-flow for various pulsating frequencies	6
6. Some typical velocity traces at $Z = 3d_j$	7
7. Typical velocity flow-field within a ring at $Z = 3d_j$	
(a) through (i) are schematically explained in Figure 4.7(j)	8
8. Sequence of traces showing fully-formed vortex ring	10
9. Collapsed trajectory for pulsating jet	11
10. Blooming jet observed without any active control of the exit geometry.	11
11. Schematic of the shock tube used to create a pulsed flow into a high speed cross-flow	11
12. Sequence of a pulsed jet coming out of the shock tube into still air. Each frame is taken in 20 microseconds with 100 microseconds between sequential frames.	11

13. Sequence of a pulsed jet coming out of the shock tube into a 1.80 Mach cross flow of air. Initial delay time of 550 microsecond. Each frame is taken in 20 microseconds with 100 microseconds between sequential frames.	11
14. Sequence of a pulsed jet coming out of the shock tube into a 1.80 Mach cross flow of air. Initial delay time of 650 microsecond. Each frame is taken in 20 microseconds with 100 microseconds between sequential frames. . . .	11
15. Schematic of the quartz pulsed valve and the set-up for combustion of methane in air.	13
16. Combusting images of a pulsed fuel jet into ambient air at 20 Hz. Burning vortex rings are apparent.	13
17. Effect of frequency on motion and trajectory at $U_\infty = 0.125, \Gamma = 1.0$	13
18. Typical vortex ring evolution at $St = 0.35, \Gamma = 1.0, U_\infty = 0.125$	15
19. Effect of frequency on motion and trajectory at $U_\infty = 0.250, \Gamma = 1.0$	15
20. Effect of frequency on motion and trajectory at $U_\infty = 0.350, \Gamma = 1.0$	15
21. Effect of circulation on motion and trajectory at $St = 0.35, U_\infty = 0.125$	15
22. Effect of circulation on motion and trajectory at $St = 0.25, U_\infty = 0.125$	15
23. Effect of cross-flow on motion and trajectory at $St = 0.35, \Gamma = 1.0$	16
24. Effect of cross-flow on motion and trajectory at $St = 0.25, \Gamma = 1.0$	16
25. Time evolution of jet pulses, issued in a uniform cross-flow, and the formation of vortex rings.	16
26. Time evolution of jet pulses, issued in a shear cross-flow, and the formation of vortex rings.	16

Tables

Table 1 Quantitative data from hot-film measurement	9
Table 2 Comparative data on vortex ring formation	10

1. Introduction

Efficient mixing of two fluids frequently plays a major role in fluid engineering problem affecting combustion, propulsion, petrochemical, food engineering, and environmental applications. In these applications, a fluid is frequently introduced in the form of a jet into a main flow. The spread of a fluid jet into an ambient stream occurs at a fixed rate which is to slow under certain conditions. As a result, mixing enhancement techniques are frequently introduced into transverse jet flows to increase the mixing rate between the jet and the surrounding fluid. Fric and Roshko (1989) investigated different types of vortical structures which exist in the near field of the transverse jet. They showed that the wake vorticity comes from the cross-flow boundary layer, and not from the jet fluid. The result of their experiment implies that the wake may not significantly contribute to mixing. Broadwell and Breidenthal (1984) noted that the transverse jet appears to be a better mixer of jet and cross-flow than a free jet. An important technique for enhancing the mixing of axial jet flows has been to introduce different periodic disturbances into the mixing process to increase the rate of mixing. Pulsation of axial jets for mixing enhancement was first introduced through the development of the pulse jet engine (Lockwood, 1963). He noted the generation of vortex rings by pulsating flow. Vandsburger et al. (1986) also observed the formation of large-scale vortex rings in the flame zone by exciting a laminar flame at a frequency of 16 Hz. This problem has received increased attention in terms of mixing improvements (Sarohia and Bernal, 1981; Reynolds and Bouchard, 1981; and Bremhorst and Harch, 1979).

As another efficient means to enhance the mixing process through deeper penetration and increased entrainment rate, Wu et al. (1988) introduced a transverse injection with forced pulsation into a uniform cross-flow with unsteady effects. Introducing unsteadiness in the jet of such flows generally resulted in flow patterns and features which were totally different from those of a steady jet and which could be of considerable value in improving the mixing rate and increasing the entrainment and diffusion of jets in cross-flow. The

objective of the present study was to investigate the increased mixing due to the pulsation of the jet in cross-flow. At low frequencies, vortex rings are formed penetrating into the cross-flow with relatively high speeds. In order to accomplish the above purpose, we need to understand the basic mechanism for vortex ring formation, dynamics and penetration into the cross-flow.

Vortex ring formation and motion have been the focus of research by many investigators for over a century ever since Helmholtz (Thomson, 1883) formulated the general vortex theorems. The motion of vortex rings is one of the interesting fluid phenomena with concentrated vorticity. The fact that a vortex ring can transport fluid and momentum over a certain distance has been one of the motivations for vortex ring research. The early works on the vortex ring phenomena are well described in the paper by Guhler and Sallet (1979). These early studies (Thomson, 1883 and Hicks, 1885) are based on the following simplifying assumptions; the ratio of core radius to ring radius, a/R , is very small and the vorticity is concentrated in the vortex core. Magarvey and Maclatchy (1964) used photography to extensively investigate the formation, structure and disintegration of vortex rings by flow visualization with smoke in air. The propagation property of vortex rings in air has been investigated by using stroboscopic photography and hot-wire anemometry by Johnson (1970). The study was devoted to accurately measuring the decay of real vortex rings in quiescent air and comparing calculated ring behavior with the various theoretical predictions. Sallet and Widmayer (1974) measured the characteristic features of laminar and turbulent vortex rings with hot-wire anemometers. These measurements were comprised of the translational velocity, ring diameter, core diameter, and circulation at several points downstream from the orifice exit. The thorough discussion of the structure and stability of viscous vortex rings was qualitatively performed in a series of papers by Maxworthy (1972, 1974, 1977). Using flow visualization and laser doppler velocimetry he investigated the formation process, vorticity, the flow fields, the translational velocity, and stability of vortex rings over a wide range of Reynolds numbers. The temporal development

of the rolling-up process of vortex rings was investigated in detail using flow visualization and laser doppler velocimeter by Didden (1979). He examined the variation of velocity, diameter, and circulation of vortex rings which move between the point of formation and a location three jet diameters downstream.

Many studies have been performed based upon vortex methods to simulate a vorticity-dominated flow of an incompressible, two-dimensional flow since Rosenhead (1931). Even though the method has some inherent difficulty that has limited the application of the method, it is generally known that the rotational region of fluid motion is well simulated by a number of discrete vortex filaments in an inviscid flow. A vortex ring is a typical example of vorticity-dominated flow with a small compact region of vorticity. There have been a number of simulations of two-dimensional axisymmetric vortex rings performed; but, some studies were done on three-dimensional vortex ring configuration with variations of size, position, and shape considered together. A series of vortex rings can be simulated by the three-dimensional discrete vortex method and the time dependent motion of each of the discretized vortex elements can be traced throughout the flow field with this computational methodology. Detailed analysis and review of the discrete vortex method have been given by Leonard (1980, 1985), Ashurst and Meiburg (1988) and Sarpkaya (1989) in modeling jets, wakes, boundary layers, vortex rings, and other vorticity-dominated flow.

To the authors' knowledge, there has not been a systematic study of the dynamics of vortex rings in cross-flows. Therefore, this study was divided into two parts. First, through an experimental investigation, the vortex rings produced by pulsed transverse injection into a uniform cross-flow were studied using flow visualization techniques and hot-film anemometry. Second, a numerical simulation for three-dimensional vortex rings in cross-flows was carried out using the Lagrangian, grid-free, vortex method to help understand and to compliment the experimental results.

2. Experimental Procedures

2.1 Description of the Water Tunnel Facility

The water tunnel, located at The University of Tennessee Space Institute, is a closed-return type and the dimensions of the test section are 30.5 cm high, 45.7 cm wide and 150 cm long (12 in \times 18 in \times 60 in). The tunnel speed can be varied from 1.5 cm/sec to 60 cm/sec. The test section walls are constructed of 1.27 cm thick Plexiglas for versatility in observing and photographing the flow field. The measured turbulence intensity in the test section was measured as 0.1%. The nozzle between the stagnation chamber and test section is a bell mouth type, which gradually and continuously changes from a circular to rectangular cross-section with a contraction ratio of 13.5. The tunnel velocity field was calibrated by using a cylindrical hot-film probe to ensure uniform cross-flow. The probe was calibrated by using a specially constructed water channel (Chang, 1991).

2.2 Experimental Setup for Continuous Pulsation

Figure 1 shows the schematic of the experimental setup in the water tunnel. The jet was installed on a false floor of the test section which provided a known boundary layer at the jet location. The false floor was a surface-finished plate with an elliptic leading edge whose aspect ratio is 2:1 and it was located 19 mm above the tunnel floor and was 1500 mm long. The jet exit ($d_j = 12.7$ mm) was located 190 mm behind the leading edge. This allowed the laminar boundary layer thickness at the jet to be on the order of one jet diameter. The Reynolds number based on the jet diameter and steady jet velocity was $Re_{d_j} = 1.87 \times 10^3$. The tunnel floor and one side wall were marked, using a square grid pattern, with lines spaced at equal distance to be used with the flow visualization data collection of vortex rings size and trajectories.

Pulsation of the full jet flow was accomplished by incorporating a solenoid valve inline in the water supply tube. This valve was driven by a frequency generator so that any frequency pulsation could be investigated. The valve did not respond uniformly at frequencies of 20 Hz and above. The solenoid valve was approximately 20 diameters upstream of the jet exit; thus, ensuring a uniform pipe flow at the jet exit (Chang, 1991).

The motion of vortex rings was studied for several different area-averaged jet exit velocities to cross-flow velocity ratios, $\bar{U}_j/U_\infty \simeq 1.5$ to 6.7. The jet-equivalent velocity was 14.88 cm/sec which is a velocity without pulsation in the pipe. The pulsed jet was maintained at a flow rate of 18.85 cm³/sec (0.3 GPM), therefore, the variations in \bar{U}_j/U_∞ were obtained by the changes in the cross-flow velocity U_∞ . The jet-equivalent velocity in the pipe should be distinguished from the jet exit velocity, (\bar{U}_e), caused by the pulsation in the same pipe. This jet exit velocity was close to the initial translational velocity of the vortex ring.

Typical velocity traces, at the jet exit, at different frequencies are presented in Figure 2. The original pulsed velocity profile generated by a function generator was a square wave. The low frequencies (e.g., 1 and 2 Hz) pulsations make the flow more like a periodic train of impulsively started rings in a cross-flow rather than an excited jet in a cross-flow. The velocity trace characteristics have a significant effect on actual vortex ring formation as does the piston velocity profile in a single pulsation by the piston-cylinder assembly. As the frequency increases the maximum velocity (impulse) is considerably reduced. This means that at high frequencies the circulation of the ring is considerably decreased while a steady flow rate remained constant.

2.3 Hot-Film Anemometry and Data Acquisition

Hot-film anemometry was used to measure the velocity field and determine characteristic parameters of vortex rings in cross-flow. A single hot-film probe was utilized with anemometers operated in the constant-temperature mode to measure mean velocities in

the three-dimensional flow field. The Constant Temperature Anemometry (CTA) system is comprised of a normal TSI hot-film probe, a TSI model IFA 100 Intelligent Flow Analyzer, a Scientific Solution's Lab Master 16 channel A/D converter, a 1 kHz low band pass filter and a IBM PC with 20 megabyte hard disk. An oscilloscope was connected to the control box to observe the voltage traces obtained from measurements within the flow field.

Figure 3 represents a schematic diagram of the data acquisition system. The voltage signals from the hot-film probe were sent into the Intelligent Flow Analyzer, (IFA), which was connected to the Lab Master A/D converter. The signals passed through the 1 kHz band pass filter to eliminate noise. The signals were digitized and were sent to a VAX 11/785 computer for storage and processing to obtain the velocity components from the calibration results.

Probe calibration is described in Chang (1991) with a discussion of directional characteristics of a hot-film probe. Also, general expression for the effective cooling velocity of a probe in the three-dimensional flow field is derived for the interpretation of the anemometer output signal.

2.4 Flow Visualization Techniques

Two types of flow visualization techniques were utilized for water tunnel experiments to complement each other for a complete description and analysis of the flow details. The techniques unveiled the global flow features of vortex rings in cross-flow. The flow was visualized using a common dye technique. The dye was a mixture of commercial food coloring, alcohol, and evaporated milk with a specific gravity of one. Internal dye ports were built into the jet exit region to allow flow visualization with minimal disturbance into the local flow and, therefore, the vortex rings were colored. Both a camcorder and conventional 35 mm camera with 1/1000 sec frame setting were used to take pictures.

A laser light sheet technique was applied to provide a sectional view of the vortex rings. An Argon ion laser light source with a maximum power output of 2 watts was used for the laser sheet visualization. A 45° inclined mirror and a 4 mm cylindrical lens were employed to reflect and produce a plane laser light sheet. Rhodamine 6G fluorescent dye was supplied in small concentrations through four small holes around the nozzle to coordinate the pulsing fluid. Sectional views of the vortex ring were obtained to analyze the detailed structure of the ring and its wake.

2.5 Measurement Uncertainties

The experimental uncertainties associated with measurements of the mean jet velocity (\bar{U}_j), sensor operating temperature (T_s), corrected effective cooling velocity ($\bar{U}_{eff,c}$), time-averaged mean velocity components (\bar{U} and \bar{W}), the measurement of circulation (Γ_m) and ring size (R) were estimated for a typical vortex ring at a frequency of 1 Hz the $Z = 3d_j$. Following are the experimental uncertainty estimates of the above properties actually measured. $\Delta\bar{U}_j : \pm 11.0\%$ (this is a maximum possible error, based on usual error analysis, and in reality could be much less), $\Delta T_s : \pm 0.15\%$, $\Delta\bar{U}_{eff,c} : \pm 0.57\%$, $\Delta\bar{U} : \pm 2.82\%$, $\Delta\bar{W} : \pm 0.60\%$, $\Delta\Gamma_m : \pm 12.42\%$, $\Delta R : \pm 4.57\%$. These estimates are valid for all vortex ring cases with the same odds. The uncertainties in the calculated value was evaluated using the standard uncertainty equation (Kline and McClintock, 1953) based on the uncertainties in the primary measurements (Chang, 1991).

3. Experimental Results

3.1 Motion of Vortex Rings in Crossflow

Figure 4 shows selected still photographs which reveal several characteristic vortex ring features observed in the present study such as the size, tilting, and trajectory of the vortex rings while moving in the cross-flow. From these observation it was evident that vortex rings, for the range of parameters in this study, move as blobs of fluid with little change in their shape. The tilted shapes and wake structures of the vortex rings were identified using laser-induced fluorescence (LIF) flow visualization. The core of the vortex ring is defined as the region where the velocity varies linearly with the distance from its center. A wake region, where a small amount of the ring fluid, therefore vorticity, is left, also exists behind the ring.

As the pulsation frequency increased in this experiment, two separate physical phenomena were seen to influence the vortex rings and their trajectories. First, the circulation strength within each ring was reduced, which directly resulted in the reduction of its induced translational velocity. This enabled the cross-flow momentum to overcome each ring easily and deflect it into the downstream. Second, the distance between the sequential rings reduced as the frequency increased. This resulted in interactions between the rings, such that the vortex rings quickly coalesced.

In this case, when two sequential vortex rings are close to each other, the vortex ring diameter of the forward vortex ring increases with decreasing vortex ring velocity; the diameter of the rearward vortex ring decreases while its vortex ring velocity increases. Since this interaction is present during the initial development of the individual rings, the rings are not fully-formed as they are turned into the downstream direction. The jet flow development into the cross-flow including the jet trajectory, at high pulsing frequency of larger than 15 Hz is approaching that of the steady jet case.

Figure 5 shows the trajectories of the vortex rings at various frequencies for different jets to cross-flow velocity ratios. These vortex ring trajectories exhibit two fundamental results. First, the penetration level at low frequencies is much higher than at high frequencies for the constant jet to cross-flow velocity ratios: second, for a given pulsing frequency the penetration height decreases as the jet to the cross-flow velocity ratio decreases.

3.2 Tilting Mechanism for a Vortex Ring in Crossflow

Vortex rings are generated by the periodic opening and closing of a valve in the supply line into a cross-flow environment. Vortex rings are formed at the exit of the line, if the opening and closing takes place in short time pulses. At low frequencies, rings are distinctly separated from each other with minimum interactions. Vortex rings produced in this manner move as unit blobs for several diameters into the flow. The motion is interesting in that it involves tilting of the ring into the cross-flow. The tilting process was initially believed to be related to the interferences which might exist between sequential rings. However, experiments showed that even for a single vortex ring there was an appreciable amount of tilting present as it moved from the exit into the cross-flow. Figure 4(f) shows the motion of a single vortex ring into a uniform cross-flow. The tilting is most pronounced for rings with small circulation, generated with a short stroke. At higher frequencies the rings are weakened and are spaced very close to each other and the tilt is increased, thus, the interaction between adjacent rings could also affect the tilting. Pulsation frequency affects circulation, size, and translational velocity of the rings, therefore, for each pulsation frequency the vortex ring will be formed with a different range of flow variables.

The tilting mechanism of a vortex ring in cross-flow may be explained using a qualitative approach. At low frequencies they are assumed to be non interfering: therefore, each vortex ring may be analyzed individually. Ting and Tung (1965) used a spinning solid cylinder as a model for the dynamics of a fluid vortex core with uniform vorticity. They used the Kutta-Joukowski theorem to calculate equivalent forces on the vortex core.

However, Caruthers (1991) has suggested that a Rankine vortex model is kinematically inconsistent with the Kutta-Joukowski result and that a singular layer of vorticity on the surface of the circular cylinder should be added to the model in this case. Superimposing a constant vorticity within the cylinder (Rankine vortex) serves to transport the surface layer vorticity as a solid cylinder rotation of the initial distribution and its potential field. He suggested that the implied lift on the fluid within the circular cylinder obtained, based on this assumption, was only one half of the Kutta-Joukowski result for a solid body. Even though there still exists a controversy about the magnitude of the forces and the tilting mechanism, the acting force is proportional to the Kutta-Joukowski result with the realization that the actual forces depend on the details of the actual core and layer vorticity distribution. A non uniform interaction with the cross-flow leads to the tilting of the ring as it is formed near the jet exit. The tilting then results in the upstream travel of the ring as it moves into the cross-flow, as shown in Figure 4(f). This figure represents a single ring moving into the cross-flow of the tunnel. There are no other vortex rings in the flow and the tunnel flow is uniform except for a relatively thin boundary layer on the tunnel floor. The tilting and subsequent upstream motion of the vortex ring is evidenced from the trailing dye.

3.3 Quantitative Measurements

A large amount of the research into vortex rings is based upon flow visualization, and are therefore, to some extent, descriptive and subjective. There have been relatively few quantitative studies to measure the detailed structure of the ring. The circulation, vorticity distribution, core size, and translational velocity can be determined throughout the ring from measurements of the velocity components. In order to better understand some of the above-mentioned specific features, it was necessary to investigate the quantitative characteristics. In this section, the results of hot-film measurements are discussed.

To illustrate the present quantitative measurements, a typical vortex ring in the cross-flow was selected with a velocity ratio, $\bar{U}_j/U_\infty = 3.0$, and a frequency, $f = 1$ Hz where no interaction between neighboring vortex rings exists. The velocity field (\bar{W} and \bar{U}) of the ring in cross-flow was measured at three different locations ($Z = 3D_j, 7D_j$ and $10d_j$). The mean pulsating velocity (\bar{u}) at $f = 1$ Hz was 12.63 cm/sec which corresponds to the velocity ratio, $\bar{u}/U_\infty = 2.4$ in this case. A single hot-film probe was used to measure two velocity components, \bar{W} and \bar{U} , at a fixed point as the vortex ring passes by the measuring point. Two velocity components are measured by rotating the plane of the prong through 90° . The first probe position selected was parallel to the cross-flow ($\theta = 0^\circ$) and the other probe position was perpendicular to the cross-flow ($\theta = 90^\circ$) in the $Y-Z$ plane.

The tilting angle of the vortex ring was determined by measuring the time difference between the peak velocities at the front inner edge and rear inner edge of the ring. The tilted angle measured by this method was about 3° at $Z = 3d_j$. The center position of the ring was $X = 0.40d_j$ at $Z = 3d_j$, which means the ring moved slightly toward the stream wise direction due to the cross-flow. Some typical velocity-time traces along the radial positions at $Z = 3d_j$ are presented in Figure 6. The velocity-time traces were obtained by using a $\theta = 0^\circ$ hot-film probe. Figure 6(a) shows a typical velocity-time trace when the center of the vortex ring passes by the hot-film probe. The dip is caused by the rotational motion of the ring core. Figures 6(b) and (c) indicate typical velocity traces at the inner edge of the ring core and the center of the vortex ring, respectively.

Tests were repeated from four to eight times at each of three downstream locations to ensure the repeatability of the results and to obtain the averaged data in the analysis. Hot-film measurements at $Z = 10d_j$ were much more difficult to do than at $Z = 3d_j$ due to the various ring trajectory from run to run. It has already been noted that some data scatter was observed relatively far downstream in the flow visualization results. It appeared that the data scatter might be due mainly to a slight non-uniformity in pulsations generated by

the combination of the solenoid valve and the frequency generator. Therefore, great care was especially taken at these point measurements to minimize their effect.

Figure 7 represents some typical non-dimensional velocity profiles \bar{W}/U_T and \bar{U}/U_T versus the non-dimensional coordinate Z/D (D is a ring diameter) which corresponds to the time that a vortex ring passes through the probe at $Z = 3d_j$. As mentioned above, the ring was surveyed along nine radial positions. Here, the distribution of each velocity component is transformed to the steady coordinate system by converting t -coordinate to Z -coordinate using $Z = U_T \cdot t$, where U_T is the instantaneous translational velocity of the ring at a measuring point. Data was collected at a rate of 600 samples per second. The translational velocity U_T and the ring diameter D at the measuring point were selected as characteristic parameters. The assumption of quasi-steady motion implies that the properties of a vortex ring are not significantly changed by the cross-flow and/or wakes during the time that a vortex ring passes by a measuring point. Since the hot-film probe cannot detect the negative velocity component, the negative velocity profiles in Figure 7 are resolved by flow visualization.

In order to determine the translational velocity, core diameter, ring diameter, and circulation, several different methods can be adopted. Locations of vortex ring core centers were very carefully determined from traces like those in Figure 6(a). Near the core center, the probe was moved in small increments of 0.0156 cm to be able to detect the core center position as accurately as possible. For example, the core diameter at $Z = 3d_j$ was repeatable to within a maximum $\pm 4\%$ (Chang, 1991). Then, the inner edge and outer edge of the core were determined from the inner peak velocity point. The core radius between the position of peak velocity and core center was decided by assuming that the core is exactly circular in shape by having circular streamlines. It was confirmed that the core diameter obtained from the above method is equivalent to the distance between peak velocities. The peak velocity at the inner edge U_{ie} , is the sum of rotational velocity U_{rot} and the translational velocity U_T . Also, the outer edge velocity, U_{oe} , is the difference

between U_{rot} and U_T . Therefore, the translational velocity and rotational velocity of the core can be calculated as follows:

$$U_T = \frac{1}{2}(U_{ie} + U_{oe}) \quad (1)$$

$$U_{rot} = \frac{1}{2}(U_{ie} - U_{oe}) \quad (2)$$

The effective core circulation can be calculated from the core rotational velocity.

$$\Gamma_c = U_{rot} \cdot 2\pi a \quad (3)$$

The total measured circulation was evaluated by integrating the velocity profiles \bar{W} as a function of Z along the vortex ring centerline. Hence, we can calculate the amount of vorticity contained within the core. In this case, Γ_c/Γ_m was estimated to be about 65.5% at downstream locations, where Γ_m is the total measured circulation obtained from velocity profiles \bar{W} .

Table 1 presents a summary of quantitative data obtained from hot-film experiments at three different downstream locations for $f = 1$ Hz pulsation. The Reynolds number based upon the ideal circulation, Re_{Γ_i} , was 3970 in this case. Γ_i indicates the initial ideal circulation calculated using the simplified slug model which is a predicted value. Γ_i was computed by using the following relation with the exit velocity profile of Figure 2.

$$\Gamma_i = \frac{1}{2} \int_0^T \bar{u}^2(t) dt \quad (4)$$

where $\bar{u}(t)$ is the mean pulsating velocity of the fluid ejected through the exit. The amount of measured circulation almost linearly decreased as the ring moved downstream.

We need to discuss an important point concerning the relationship between measured core circulation and measured total circulation. Also, it is significant to highlight the discrepancy between the measured circulation and ideal circulation using a simple slug model. Maxworthy (1977) noted that only about 50% of the total circulation is contained within the core at high Re_M based on the exit velocity and exit diameter. Contrasts

between the present study and the theoretical result of Sallet and Widmayer (1974) who obtained 65.5% and 71.5% of concentration within the core, respectively. Maxworthy (1977) also found that the total of a measured amount of vorticity that appears downstream is very close to that predicted by a simple slug model at high Reynolds number (between 10^4 and 10^5). However, Didden (1977), using Laser Doppler Velocimeter data, observed that Γ_i underestimates the total measured circulation by 30% to 60% at low Reynolds numbers until $Re_M = 6.6 \times 10^3$. In this case, the piston velocity profiles were utilized to calculate Γ_i . This also indicates that the simple slug model cannot be a good parameter to describe the formation process. Finally, it can be seen that the above relationship between core and measured circulations depends on a given piston motion and/or pulsed frequency and exit geometry. In Didden's experimental work, the measured circulation is much larger than the ideal circulation using the simple slug model. Didden (1979) explained in detail the factors that can increase the circulation above the ideal value as follows; one is due to a much larger velocity than the exit velocity, near the sharp corner at the nozzle exit for short times; the other is due to the accelerated core flow for constant piston velocity by a thicker internal boundary layer. In the present study, the total measured circulation was very close to the ideal circulation using the slug model. At $Z = 10 d_j$, it deviated only 15.7% from the ideal quantity.

The tilting angle slightly increased as the ring moved downstream, however, it was observed that the tilting angle of a ring tended to be restored to the horizontal orientation farther downstream (near the free surface) even though it was not quantitatively confirmed by a hot-film probe experiment. The average tilting angle, for the range of flow parameters in this study, was estimated to be approximately 3° to 4° during the vortex ring movement in the cross-flow. Higher tilting angles of up to 30° were observed for slower flow rates. The expression for translational velocity by in viscid flow theory is expressed as follows:

$$U_T = \frac{\Gamma}{4\pi R} \left\{ \ln \left(\frac{8R}{a} \right) - \frac{1}{4} \right\} \quad (5)$$

which is comparable to the quantity from vortex ring measurements, a non-dimensional velocity was introduced as

$$\tilde{U} = \frac{4\pi R U_T}{\Gamma_M} \quad (6)$$

The above equation is equivalent to $\ln(8R/a) - 1/4$ in the in viscid equation. Under the present experimental range, the deviations from the real value was reasonably small. This makes sure that the results using equation (5) for $A = 1/4$ for a viscous vortex ring is accurate within 30%.

3.4 Measurement of a Fully-Formed Vortex Ring

In order to quantitatively investigate the distance from the exit a fully-formed vortex ring is produced, traces of point-wise velocity versus time histories were obtained at twelve different locations (from the exit to $Z = 4d_j$) along the jet exit centerline. The data shown in Figure 8 indicate that the ring is basically fully-formed at $Z = 3D_j$ downstream from the exit. Up to $Z = 2d_j$, the velocity traces look like jet flow movement without forming a real vortex ring. The velocity travels between $2d_j$ and $3d_j$ are considered in this study as showing the formation processes of a vortex ring. When a fully-formed vortex ring is passed through the hot-film probe, the velocity profile became symmetric about a peak velocity, e.g., after $Z = 3 d_j$, as shown in Figure 8. After the ring passed downstream of $Z = 3 d_j$, no change in the configuration of its continuing formation process was observed. Whitehead (1968) numerically investigated the vortex ring formation process up to five exit diameters. He suggested that $2d_j$ is enough distance to obtain a fully-formed vortex ring. Sallet and Widmayer (1974) observed by photographic study that the rings are formed within about $2.5d_j$ from the vortex generator. They also noted that the early development of fully-formed vortex rings seem to be independent not only of the piston speed but also holds true for vortices formed with different piston velocity profiles.

Table 2 presents some comparative data on vortex ring formation. In Table 2, the Reynolds number is defined as $Re_j = \bar{u}R_j/\nu$, where R_j is the exit radius, \bar{u} is the exit flow

velocity and ν is the kinematic viscosity of the medium used. Whitehead (1968) used the peak pulsating velocity, while the mean pulsating velocity was selected as \bar{u} in Sallet and Widmayer's work (1974) and the present study. It also appears that there is no significant effect of cross-flow on vortex ring formation under the present experimental range.

3.5 Dimensional Analysis for Pulsating Jet Trajectories

If the data for the different velocity ratios (\bar{U}_j/U_∞) are collapsed onto a single line, simple power law relations describing the pulsating jet trajectories in the cross-flow can be easily determined. This approach is composed of the combination of dimensional analysis and fundamental physical arguments about the characteristics of each jet flow. First of all, an appropriate length scale associated with the jet flow characteristics needs to be defined.

In the present study, the dependent parameter of major importance is the penetration of the vortex ring in the vertical direction. It can be described by the following function

$$g(\bar{U}_j, d_j, U_\infty, U_T, \nu, Z, X, t, f, l_d) = 0 \quad (7)$$

where f is a pulsating frequency, l_d is the separation distance between adjacent vortex rings. Dimensional analysis gives

$$g\left(\frac{U_\infty^2}{\bar{U}_j^2}, \frac{f l_d}{U_T}, \frac{\bar{U}_j d_j}{\nu}, \frac{Z}{d_j}, \frac{X}{d_j}\right) \quad (8)$$

in which the Strouhal number is defined as

$$St \equiv \frac{f \cdot l_d}{U_T} \quad (9)$$

The selection of l_d and U_T rather than d_j and \bar{U}_j for the definition of Strouhal number is that the vortex ring motion is more dependent on translational velocity and separation distance than jet velocity and diameter.

For pulsed jets, the Reynolds number based on the pulsation velocity may be relevant in the formation of vortex rings. However, since no efforts have been made on the Reynolds number effect in this study, it will be omitted from here on.

Therefore, the penetration can be described by

$$\frac{Z}{d_j} = G \left[\left(\frac{f \cdot l_d}{U_T} \right), \left(\frac{\bar{U}_j^2}{U_\infty^2} \right), \left(\frac{X}{d_j} \right) \right] \quad (10)$$

The vertical trajectory of a vortex ring jet is expected to depend on the Strouhal number based upon translational velocity and separation distance between adjacent vortex rings and the momentum flux (\bar{U}_j^2/U_∞^2).

In order to correlate the pulsating jet flow penetration for different jet free stream velocity ratios and various frequencies, a modified frequency-momentum length scale is introduced similar to the steady case

$$l_{f_m} = d_j \left(\frac{\bar{U}_j^2}{U_\infty^2} \right) \left(1 + \frac{\kappa U_T}{l_d f} \right) \quad (11)$$

where κ is a similarity parameter to be determined through a least square fit of the data. The data of Chassaing et al. (1974) was fitted using a regression process. In this calculation the κ resulted as 3.8. The result in Figure 9 indicates a good correlation of all the various data. This correlation is being considered as a new similarity coordinate. From the match between experimental results and similarity analysis, we can estimate that the effects of both excitation and the ratio of momentum flux (\bar{U}_j^2/U_∞^2) on the trajectory are dominant for the pulsating jet. It has been well known that the momentum flux ratio (\bar{U}_j^2/U_∞^2) is one main parameter correlating the characteristics of the steady jet in a cross-flow.

3.6 Blooming Rings

An interesting observation was obtained in the course of investigating the vortex rings in cross-flow. At very low cross-flow speeds ($\bar{U}_j/U_\infty \geq 3$) and for 10 Hz frequency the vortex ring trajectory was not stable and the rings were found to frequently move in various directions into the cross-flow and into the upstream direction, in a lateral direction and the various orientations, Figure 10. The resulting flow appeared like a blooming jet obtained by combined axial and orbital excitations (Lee and Reynolds, 1984). These observations

confirmed that a blooming jet can be generated by implementation of a certain geometry to provide passive helical excitation coincident with a resonance mode of the pipe without active orbital excitation. The divergence angle is a reflection of the amplitude of the orbital (helical) excitation. The divergence angle of the blooming vortex rings was smaller than that of Lee and Reynolds (1984). The mechanism for blooming jets and bifurcating jets is discussed by Parekh et al. (1988) and Lee and Reynolds (1984). The prominent mechanism for these particular excited jets is known to be due to the interaction of the vortex with the initial conditions.

Anderson (1955) reported in a paper on the structure and velocity of the periodic vortex ring pattern of a Pfeifenton (Pipe Tone) jet. He found different and very unusual vortex flow patterns, which showed an amazing and reproducible splitting of the jet into two distinct circular vortex trains (bifurcating jet) at around 1150 cps. In his paper he described the phenomena without explanation of the mechanism — this supports the notion that it is possible to obtain bifurcating and/or blooming jets by passive excitation as shown in this experiment. This is important in helping to understand how the rings are generated in such excited jets.

4. Combustion of Pulsed Fuel Jets

Based on the experimental and numerical results obtained (to be discussed in the next section) it is reasonably clear that, if the flow is pulsed such that vortical rings are formed as the jet is issued into the cross-flow, then increased penetration is assured. However, two questions still persisted: one, Will vortex rings also be formed once a jet is pulsed into a supersonic cross-flow? and two, What will be the combustion effect on the rings? To find an answer to these questions the following experiments were performed.

Pulsed jet injection into a supersonic cross-flow was attempted to investigate possible formation of vortex rings. An extensive search for a reasonably sized, fast response, commercially available valve was not successful. In the absence of an off-the-shelf valve to pulse the flow, a small free piston shock tube with an exit diameter of 1.25 cm was designed and manufactured, Figure 11. The tube was installed in the tunnel such that its main axis was perpendicular to the tunnel stream wise direction. High speed schlieren photography with a spark light source revealed the leading shock details, wake structures, and the jet evolution as flow emerged from the open end of the shock tube. A fast speed camera was optically coupled with the shock tube to record the injection process. The camera took eight pictures with 100 microseconds delay between two sequential photos. The starting trigger mechanism for the camera could be timed for different initial delays, this was necessary because of the desire to record various phases of the jet issued into the cross-flow.

Figures 12, 13 and 14 show the sequence of a pulsed flow out of the tube into the tunnel with and without supersonic flow. A delay time was used to allow the jet to leave the tube, before it is photographed. In these figures the time delay for the camera was about 500 to 650 microseconds, each frame is taken in 20 microseconds, and each frame is separated from the next by a time interval of 100 microseconds. As the flow is emerging from the jet exit (frame 2) at high speeds, a shock wave is formed. However, behind the shock wave appears to be a turbulent mushroom shape ring vortex. This is interpreted

to be a supersonic vortex ring which we have intended to generate. The development of this single pulsed jet flow can be traced in sequential photos shown in this figure (frames 2 through 8). Figure 13 shows a similar vortex process within the tunnel with cross-flow of nominal Mach 1.8 established. In Figure 13 the initial time delay is slightly more and the flow is leaving the jet exit in the first frame. As expected, an oblique shock is formed just upstream of the jet exit flow. Even though the pictures are not so clear, a supersonic vortex ring (mushroom) is visible in the jet flow. The ring is only clearly visible in the frames 1 and 2 of the Figure 13. From the shock structure deformation, the approximate position of the ring can be approximately identified. Figure 14 shows another shot similar as the one in Figure 13, except with an initial delay time of 650 microseconds. There appears to be strong similarities between the behavior of vortex rings in supersonic flow and that of low speed flows considered earlier.

A valve capable of being continuously pulsed at very high rates, orders up to kilohertz, and necessary to maintain combustion could not be found commercially. An effort to design an in-house valve was abandoned after it was realized that it may become a project of uncontrolled and large magnitude by itself. There could be no comparison made with the steady jet flow for the penetration into the cross-flow, since the injection mechanism would not lend itself to be used as a steady state flow. It is believed that sufficient and accurate data for steady flow injection into a supersonic cross-flow exists and could be used for comparison, if needed. For example, these would be consistent with the previous data on Figure 9.

Therefore, an effort was undertaken to study the combustion of a pulsed propane fuel jet in ambient air. The main point being the investigation of vortex rings formation and motion during the combustion process. A setup using the piezoelectric valve, (General Valve model 9), noted earlier, was used to investigate the evolution of pulsed propane (C_3H_8) jets. A high voltage electric arc, between two thin copper needles, Figure 15, at the exit of the jet, was used as the spark to initiate combustion. As noted earlier, here too,

the intent was to determine, if coherent structures such as vortex rings are formed during combustion due to the pulsation of the fuel jet into the ambient flow. A Kodak fast video recorder, at the rate of one thousand frames per second was used to record images of the pulsating methane gas into the ambient air. As observed from images shown in Figure 16, one can only cautiously identify the burning puffs of the fuel as a vortex ring, even though periodically there are clean puffs resembling a burning turbulent vortex ring. Results of this visual step could be tainted because the mechanism with which the combustion was initiated was two dimensional and not axisymmetric. However, there is clear evidence that under certain conditions, vortex rings are formed and that the motion of these rings in a cross-flow is of significant interest. This is relevant, since the low speed study revealed such a significant increase in the penetration in comparison with steady jets.

5. Numerical Study

The main purpose of this numerical study is to better understand the interaction between vortex rings and cross-flow, and to explain the flow visualization experiments.

Vortex rings in cross-flow represent typical three-dimensional, unsteady vortical flow. Vortex rings are usually characterized by low viscosity and concentrated regions of vorticity embedded in an otherwise potential flow. This fact allows one to discretize the compact regions of vorticity into an assembly of vortices. Vortex methods simulate this type of flow by discretizing and tracking the discretization in a Lagrangian reference frame. A simplified flow simulation was carried out using the discrete vortex method. That is, a vortex ring was modeled by a vortex filament with a number of nodes in the shape of a torus. A discrete number of nodes which lie along the vortex centerline enable one to be able to solve the deformation problem. These points are located along a given initial configuration of the ring, along with the initial conditions on the translational velocity of each mode.

Each node on the vortex ring moves with the local velocity. Therefore, once the induced velocities are known, the movement of each node during a small time step can be calculated by multiplying the local induced velocity by the time step. For this calculation, a second order Runge-Kutta method was used to iterate on the position of the nodes and therefore, improved the accuracy of the computations.

The original code was written and developed by Parekh et al. (1988) based upon the discrete-vortex method. This code was developed to investigate the effects of excitation frequency and amplitude on the spreading of the bifurcating jet. They used an analytical function to describe the source flow and discrete, computational vortex elements to represent the vortex rings formed at the jet exit. This function was modified for our study to investigate the effect of cross-flow on the vortex rings depending on axial frequency. We computed the evolution of vortex rings in the cross-flow. The advantage of the vortex

method is that no finite mesh or grid is required, and this Lagrangian nature makes it unconditionally stable to convection.

The viscosity effect was not initially incorporated in this numerical experiment. As a result, it was not possible to obtain the characteristics of three-dimensional ring configuration, including shape and size. In order to complement this defect, jet source flow was introduced, whose flow from a semi-infinite cylindrical vortex sheet is similar to that of a viscous jet issuing from a wall, Chang (1991).

5.1 Formulation and Numerical Scheme

The equations which govern an incompressible, in viscous flow are Euler's equations;

$$\frac{D\mathbf{u}}{Dt} = \frac{\partial \mathbf{u}}{\partial t} + \mathbf{u} \cdot \nabla \mathbf{u} = -\nabla p \quad (10)$$

and the continuity equation,

$$\nabla \cdot \mathbf{u} = 0 \quad (11)$$

expressing the conservation of momentum and mass, respectively.

This computational experiment is to simulate an incompressible flow field of vortex rings where only a small portion is rotational. It will be convenient to describe the above governing equations in terms of vorticity variable. Equation (10) can be rewritten in terms of the vorticity by taking the curl.

$$\frac{D\boldsymbol{\omega}}{Dt} = \frac{\partial \boldsymbol{\omega}}{\partial t} + \mathbf{u} \cdot \nabla \boldsymbol{\omega} = \boldsymbol{\omega} \cdot \nabla \mathbf{u} \quad (12)$$

$$\boldsymbol{\omega} = \nabla \times \mathbf{u} \quad (13)$$

Equation (12) is called the vorticity transport equation which explains that the vorticity moves along a particle path while it is being tilted and stretched with the evolving strain field ($\nabla \mathbf{u}$). Therefore, the term ($\boldsymbol{\omega} \cdot \nabla \mathbf{u}$) exists only in a three-dimensional flow.

The vorticity distribution from m filaments or tubes with circulation Γ in three-dimensional flow is given by

$$\boldsymbol{\omega}(\mathbf{r}, t) = \sum_{i=1}^m \Gamma_i \int_c \gamma_i [\mathbf{r}, \mathbf{r}_i(s, t)] \frac{\partial \mathbf{r}_i(s)}{\partial s} ds \quad (14)$$

where $\mathbf{r}(s, t)$ describes the space curve of the filament centerline in terms of a parameter along the curve (s). The distribution function γ_i is assumed to have the following form

$$\gamma_i(\mathbf{r} - \mathbf{r}_i) = \frac{1}{\sigma_i^3} f\left(\frac{|\mathbf{r} - \mathbf{r}_i|}{\sigma_i}\right) \quad (15)$$

where the notation of Leonard is used with σ_i (the core radius of filament i).

Once the vorticity distribution is known, the velocity induced by the vorticity in a bounding region can be calculated from the integration of Eqs. (11) and (13). We can drive using vector identity and $\nabla \cdot \mathbf{u} = 0$ that (see Batchelor⁴⁶)

$$\nabla^2 \mathbf{u} = -\nabla \times \boldsymbol{\omega} \quad (16)$$

\mathbf{u} can be expressed as

$$\mathbf{u}(\mathbf{r}) = -\frac{1}{4\pi} \int \frac{(\mathbf{r} - \mathbf{r}') \times \boldsymbol{\omega}(\mathbf{r}') d\mathbf{r}'}{|\mathbf{r} - \mathbf{r}'|^3} + \nabla \phi \quad (17)$$

where ϕ is the velocity potential related to the homogeneous solution of the above equation which is required to satisfy the boundary conditions as follows:

$$\mathbf{u} \cdot \mathbf{n} \Big|_{\text{body surface}} = 0 \quad (18)$$

$$\lim_{|\mathbf{r}| \rightarrow \infty} \mathbf{u}(\mathbf{r}, t) = \mathbf{U}_{\infty} \quad (19)$$

The resultant velocity will be split into two components based upon the uniqueness of the decomposition of a vector field.

$$\mathbf{u}_R = \mathbf{u}_s(\mathbf{r}, t) + \mathbf{u}_I \quad (20)$$

where $\mathbf{u}_s(\mathbf{r}, t)$ is a solenoidal field which is a solution of Eq. (16) and \mathbf{u}_I is an external irrotational velocity. The induced velocity of the filament at point $\mathbf{r}(s)$ on the axis is given by Biot-Savart law

$$\mathbf{u}_s(\mathbf{r}, t) = -\frac{1}{4\pi} \iiint \frac{(\mathbf{r} - \mathbf{r}') \times \boldsymbol{\omega}(\mathbf{r}', t)}{|\mathbf{r} - \mathbf{r}'|^3} dV(\mathbf{r}') \quad (21)$$

With the thin filament approximation, it reduces to

$$\mathbf{u}_s(\mathbf{r}, t) = -\frac{\Gamma}{4\pi} \int_c \frac{[\mathbf{r}(s, t) - \mathbf{r}'(s', t)] \times \frac{\partial \mathbf{r}'}{\partial s'}}{|\mathbf{r}(s, t) - \mathbf{r}'(s', t)|^3} ds' \quad (22)$$

where s describes the coordinate along the lines. The result of this locally induced velocities which in the limit of a vortex filament becomes infinite yields a logarithmic singularity in the self-induced velocity known as a general feature of a curved vortex filament in the three-dimensional flow. This causes an infinite velocity of the filament and also causes instabilities. In order to eliminate this velocity singularities, numerous cut off schemes have been introduced, (see Sarpkaya³⁶). Another difficulty with the Biot-Savart method will be the number of operations for the induced velocity calculation. Because CPU time increases considerably as the number of vortex elements increase.

The modification of Biot-Savart law is achieved by Rosenhead's³¹ method which was modified by Moore⁴⁷ later. The evolution equation for a three-dimensional, space curves $\mathbf{r}_i(s, t)$ ($i = 1, 2, \dots, N$) for N vortex filaments. The induced velocity at a point, \mathbf{r} , is calculated as:

$$\begin{aligned} \mathbf{u}_s(\mathbf{r}, t) = & \\ - \sum_j \frac{\Gamma_j}{4\pi} \int & \frac{[\mathbf{r}(s, t) - \mathbf{r}_j(s', t)] \times \frac{\partial \mathbf{r}_j(s', t)}{\partial s'}}{\left(|\mathbf{r}(s, t) - \mathbf{r}_j|^2 + \alpha\sigma_j^2\right)^{3/2}} ds' \end{aligned} \quad (23)$$

where $\alpha\sigma_j^2$ is a measure of the vortical flow region. σ_j is the core radius and can be changed depending on the distribution of vorticity. A vortex ring with a Gaussian vorticity distribution can be simulated by a single vortex filament with the above vorticity distribution, and then the self-induced velocity has correct value for $\alpha = 0.413$, (Leonard³⁴). Therefore, this value was used for our numerical simulations. Here, α is a parameter related to the fraction of circulation within the radius $r = \sigma$ (Moore⁴⁷).

To consider the influence of vortex filament i on filament j , $\alpha\sigma_j^2$ can be replaced by $\alpha(\sigma_i^2 + \sigma_j^2)/2$ as follows:

$$\mathbf{u}_s(\mathbf{r}_i, t) =$$

$$-\sum_j \frac{\Gamma_j}{4\pi} \int \frac{[\mathbf{r}_i(s, t) - \mathbf{r}_j(s', t)] \times \frac{\partial \mathbf{r}_j(s', t)}{\partial s'}}{\left[|\mathbf{r}_i(s, t) - \mathbf{r}_j|^2 + \alpha'(\sigma_i^2 + \sigma_j^2)\right]^{3/2}} ds' \quad (24)$$

As mentioned before, $\alpha = 0.413$ satisfies the translational velocity of a vortex ring as far as σ_i is much less than ring radius.

Since a vortex line always consists of the same fluid particle and moves with the fluid in an incompressible flow, the core radius σ is kept uniform along each filament but varies with time to conserve a constant volume. It can be expressed by

$$\frac{d}{dt}(\sigma_i^2 R_i) = 0 \quad (25)$$

where $R_i(t)$ is the instantaneous length of the vortex ring filament i . The size of the core radius can vary with the local stretching of the ring. The total circulation assigned to a vortex segment at each simulation maintains constant.

5.2 Calculation Procedures

The dynamics of vortex ring in cross-flow is characterized by three-dimensional configuration which has variations with location, size and shape. For this simulation, a set of nodes (vortex elements) are incorporated to represent each vortex ring. The spacing between node points was sufficiently small so that length scales of interest would be represented accurately.

For numerical purposes, it is assumed that the core radius of each filament is much smaller than the ring radius. Therefore, the distribution of vorticity is almost Gaussian in magnitude and the vortex lines are parallel at each cross section normal to the filament tangent vector.

Since each vortex element moves with the local fluid velocity, the self-induced velocity field obtained from Eq. (24) can be integrated in time to find the subsequent location of the vortex elements. Again using Eq. (24) the velocity field at the next time can be computed and this procedure repeated.

The total velocity induced by a multi-segment filament is obtained by summing the induced velocity of each filament. The detail calculations for the induced velocity by all the vortex filaments are given in Parekh.⁴⁵

The first vortex ring is generated at the origin with the initialization of frequency and time integration parameters. Then, subsequent vortex rings are generated at given distances depending on axial frequency. The circulation of each filament has the same magnitude and is determined by circulation conservation laws. The flux of vorticity in the boundary layer (sheet) is given by $U^2/2$. It is also assumed that the vorticity convected from the cylindrical sheet equals the vorticity convected by the discrete filaments. The conservation constraints show

$$\frac{\Gamma}{\Delta t} = \frac{\gamma^2}{2} \quad (26)$$

in which Γ is the circulation of each ring filament, γ is the circulation per unit length of the cylindrical vortex sheet, and Δt is the time interval between generation of vortex ring filaments.

At each time step, the total velocity at each node due to the combined effects of the vortex segments, jet source flow and external flow is calculated. Both the spatial and the temporal integration are carried out with the second-order, Runge–Kutta method, with the node points being advanced in time

$$x' = x(t) + u(t) \frac{\delta t}{2} \quad (27)$$

$$x(t + \Delta t) = x(t) + u'(t) \delta t \quad (28)$$

in which $x(t)$ and $u(t)$ indicate a node position and velocity at time t , and δt is the time increment between time steps which is typically an order of magnitude smaller than Δt .

5.3 Simulation of Jet Source Flow

The formulation presented below follows the work of Parekh.⁴⁵ In order to simulate the jet source flow, the Biot-Savart integral is applied to a semi-infinite, cylindrical vortex

sheet of finite thickness. The jet velocity function can be derived to define the mean jet flow. The simple form of equation is given by

$$u_r(\text{or}, \bar{z}) = \frac{\gamma}{2\pi\sqrt{\nu}} I(\bar{\eta}) \quad (29)$$

and

$$\begin{aligned} u_z(\text{or}, \bar{z}) = & \frac{\gamma}{2\pi\text{or}h} \left[\frac{\pi}{2} \left\{ \frac{(2 - \text{or}h)}{\sqrt{1 - \bar{\mu}^2}} + \text{or}h \right\} \right. \\ & - \frac{\bar{z}}{\sqrt{\nu}} \left\{ \frac{2}{\sqrt{1 + \bar{\eta}}} K(1 - m_1) \right. \\ & \left. \left. + (\bar{\mu} - \text{or}) T(\bar{\mu}, \bar{\eta}) \right\} \right] \end{aligned} \quad (30)$$

where

$$\begin{aligned} \text{or} &\equiv \frac{r}{R}, \\ \bar{z} &\equiv \frac{z}{R}, \\ \bar{\sigma} &\equiv \frac{\sigma}{R}, \\ \bar{\nu} &\equiv 1 + \text{or}^2 + \bar{z}^2 + \alpha\bar{\sigma}^2, \\ \bar{\eta} &\equiv \frac{2\text{or}}{\bar{\nu}}, \\ m_1 &\equiv 1 - \frac{(1 - \bar{\eta})}{(1 + \bar{\eta})}, \\ \text{or}h &\equiv 1 + \text{or}^2 + \alpha\bar{\sigma}^2, \\ \bar{\mu} &\equiv \frac{2\text{or}}{\text{or}h}, \\ I(\bar{\eta}) &\equiv \int_0^\pi \frac{\cos \theta}{\sqrt{1 - \bar{\eta} \cos \theta}} d\theta, \\ T(\bar{u}, \bar{\eta}) &\equiv \int_0^\pi \frac{\cos \theta}{(1 - \bar{u} \cos \theta)\sqrt{1 - \bar{\eta} \cos \theta}} d\theta \end{aligned}$$

The detail derivation of Eqs. (29) and (30) and integration scheme based upon the fourth-order Newton-Cotes method are described in Ref. 45.

The semi-infinite sheet of vorticity extends from $-\infty$ to origin as shown in Fig. 19. Its axis represents the jet centerline, and the end of the sheet represents the jet exit.

Here, it is assumed that the cylindrical sheet effects the motion of the filaments but there is no effect of the filaments on the cylindrical sheet. The trajectory of each filament is determined by the total velocities induced by each filament, jet source function and by a uniform cross-flow. The sheet maintains cylindrical configuration and it is not moved due to the filaments since the cylindrical sheet corresponds to a mean flow whose centerline is determined only by the position of a physical nozzle.

5.4 Numerical Results

Numerical results are presented to investigate the interaction between vortex rings and cross-flows. The remarkable features of the trajectories and motion of vortex rings with different effects of cross-flow, circulation strength, and Strouhal number are illustrated as follows.

In order to simulate the dynamics of vortex rings in a cross-flow, discrete vortex filaments are introduced to represent the vortex rings. Each vortex filament consists of 32 nodes or vortex elements, and each vortex segment moves under the action of the induced velocity of the other segments and the cross-flow. Since the variation of core radius has a very small effect on the motion of vortex rings in a cross-flow, the uniform core radius ($\sigma = 0.1$) was selected in this calculation. The non-dimensional time step for the evolution of the vortex ring was typically below $\delta t = 0.08$. Twenty-one different cases were tested to simulate as closely as possible the experimental results. The stream wise cross-flow is in the X -direction, Z is the vertical direction measured from the jet center. An initial vortex ring is generated at the origin, and then the next ring begins to evolve under the effect of the induced velocity.

In Figure 17, the numerical results show some typical and similar tilted vortex rings having the same tilted direction as in the experiment. The downstream portion of the vortex ring moves upward under the effect of non uniform interactions between the vortex ring and the cross-flow. At each time, the side and end views are represented in Figure 18.

The large value of time was used to observe the deformation of large numbers of vortex rings on each simulation. In the following subsections, the effects of pulsations through the change of Strouhal number (frequency), circulation strength and cross-flow including constantly uniform, uniform shear and non-uniform flows will be described in terms of ring trajectories and motions. The sequences of events during vortex ring evolution are shown in Figures 19 and 20 as a function of frequency. The data in each figure was given a different magnitude of uniform velocity. As the frequency increases, the spatial distance between neighboring vortex rings becomes smaller. Also, the penetration at relatively high frequency is reduced due to the strong interactions between adjacent vortex rings. This observation was revealed in the experimental work described above. Therefore, it is seen that the spatial distance between vortex rings is determined by the axial pulsation (through Strouhal number). Naturally, the total number of vortex rings generated are increased within the fixed coordinate frame as the axial frequency increases. Also, the increase of uniform velocity makes the vortex rings more deflected and consequently reduces the penetration with the same pulsation conditions. This causes the total number of rings to be decreased within the fixed frame. The averaged tilting angle in this numerical calculation is in good agreement with the measured value (about 3° to 4°) except for the case of $St = 0.35$ and $U_\infty = 0.125$.

The initial circulation strength of the vortex ring has a significant effect on the trajectories of rings in the cross-flow. As illustrated in Figures 21 and 22, the penetration of vortex rings into the cross-flow are considerably deeper with the increase of circulation strength. The circulation effect was investigated for two different ranges of Strouhal number. At relatively high Strouhal number ($St = 0.35$), as the circulation increases, a tangle of vortex rings is caused due to the strong interaction of two neighboring vortex rings as presented in Figure 23. In Figure 24 ($St = 0.25$), as expected, a considerable trend of increase of penetration was observed without entanglement by the interaction of adjacent

vortex rings. Also, the tilted configuration of the ring was not considerably changed as long as the relatively low pulsation is maintained.

We also investigated the effect of cross-flow on the vortex ring, by just adding different kinds of velocity profiles. It was discussed by Aref and Flinchem (1984) that the incorporation of the background flow is an approximation which neglects the effect of the vortex ring on the background flow. The case of uniform shear flow was considered first with $U(Z) = mZ$ where m is 0.125. Next, we impose a non uniform shear flow with the exponential velocity profile as follows,

$$U(Z) = n(1 - \exp(-Z)) \quad (12)$$

With $n = 0.125$, this profile has the same shear rate at $Z = 20$ as in the uniform shear flow case. This indicates that it has larger shear rates than the uniform shear case below $Z = 20$. The vortex ring evolution is shown in Figures 25 and 26. The uniform shear flow has more penetration due to the low shear rates, however, at relatively high Strouhal numbers it tends to easily entangle with strong interactions between adjacent vortex rings. The exponential velocity profile shows more or less close trajectories and motion of vortex rings compared to the constantly uniform cross-flow case.

Two important results are illustrated from this numerical simulation. One is the various penetrations of vortex rings due to the effect of pulsations, circulations, and cross-flows. The other is the tilted configuration of vortex rings in the cross-flow. This numerical simulation confirmed that the tilting mechanism of the vortex ring is due to the combined effect of cross-flow and the viscosity of the jet source flow. As shown in the experimental results, the basic circular shape is maintained within the fixed coordinate frame. In order to make more meaningful comparisons between numerical and experimental results, it is necessary to match basic parameters and initial conditions for the generation of vortex rings accurately. That is, at the same time t , the position and induced velocity of the vortex ring should be calculated to reasonably predict the subsequent behavior of the ring.

6. Conclusions

The following conclusions have been drawn from this research, based on the experimental observations including measurements and computational results. As a result of full pulsation of the flow of a steady jet, vortex rings were formed. At low pulsing frequencies the vortex rings penetrated into the cross-flow much deeper than for high pulsing frequencies or for the steady jet. Interactions between vortex rings became dominant at low jet to cross-flow velocity ratios and for high frequencies. No appreciable interaction was observed between neighboring vortex rings below pulsing frequencies of 4 Hz for a jet to cross-flow velocity ratio of three. The vortex rings at low frequencies moved as unit blobs of fluid with little change in their general shape. Analyses showed that pulsation frequency and momentum flux effects were two factors dominating dynamics of pulsating jet flow. Penetration trajectories of the pulsed jets (vortex rings) were characterized by a power law for each velocity ratio and pulsing frequency. Pulsation of the steady jet, therefore, resulted in increased penetration and increased mixing.

The velocity field measured within vortex rings, generated by pulsing at 1 Hz for a jet to cross-flow velocity ratio of 3.0, revealed fundamental characteristic features of single vortex rings in cross-flow. Measurements provided information that vortex rings are fully-formed at $Z = 3d_j$, which is in good agreement with the observations by others, in still air, as well as computational results. Circulation measured by the hot-film probe was close to that predicted by a simple 'slug model'. At $Z = 3d_j$, 9.2% of the ideal circulation was lost from the ring while 24.2% was lost at $10d_j$.

Computational results supported and agreed with the increased penetration of the pulsed jet and the tilting of individual rings, as observed in the experiments. As the frequency (Strouhal number) increased, the spatial distance between the vortex rings became smaller, and the penetration was reduced due to strong interactions between adjacent vortex rings as observed from the experiments.

Acknowledgements

Technical discussions with Profs. J.E. Caruthers, and T. H. Moulden have been very useful. This work was supported by the Office of Naval Research, Grant N00014-89-1696, Technical Officer Dr. G. Roy.

References

- Anderson, A.B.C., "Structure and Velocity of the Periodic Vortex-Ring Flow Pattern of a Primary Pfeifenton (Pipe Tone) Jet," *J. Acoustical Society of America*, 1955, Vol. 27, No. 6, pp. 1048-1053.
- Aref, H. and Flinchem, E.P., "Dynamics of a Vortex Filament in a Shear Flow," *J. Fluid Mech.*, Vol. 148, 1984, pp. 477-497.
- Ashurst, W.T. and Meiburg, E., "Three-Dimensional Shear Layers via Vortex Dynamics," *J. Fluid Mech.*, Vol. 189, 1988, pp. 87-116.
- Bremhorst, K. and Harch, W. II., "Near Field Velocity Measurements in a Fully Pulsed Subsonic Air Jet," *Turbulent Shear Flows I*, Springer-Verlag, Berlin, 1979, pp. 480-500.
- Broadwell, J.E. and Breidenthal, R.E., "Structure and Mixing of a Transverse Jet in Incompressible Flow," *J. Fluid Mech.*, Vol. 148, 1984, pp. 405-412.
- Caruthers, J.E., private communication, 1991.
- Chang, Y.K., "Dynamics of Vortex Rings in Cross-Flow," Ph.D. Dissertation, Univ. of Tennessee, 1991.
- Chassaing, P., George, J., Claria, A., and Sananes, F., "Physical Characteristics of Subsonic Jets on a Cross-Stream," *J. Fluid Mech.*, Vol. 62, 1974, pp. 41-64.
- Didden, N., "Untersuchung Laminar, Instabiler Ringwirbel mittels Laser-Doppler-Anemometrie," Mitt Nr. 64, Gottingen: Max-Planck-Inst., Stromungsforschung, 1977.
- Didden, N., "On the Formation of Vortex Rings: Rollin-Up and Production of Circulation," *ZAMP*, Vol. 30, 1979, pp. 101-106.
- Fric, T.F. and Roshko, A., "Structure in the Near Field of the Transverse Jet," Seventh Symposium on Turbulent Shear Flows, Stanford, CA, Aug. 21-23, 1989, pp. 225-237.
- Guhler, M. and Sallet, D.W., "The Formation of Vortex Rings and Their Initial Motion," *Z. Flugwiss Weltraumforsch*, Vol. 3, 1979, pp. 109-115.

Hicks, W.M., "Researches on the Motion of Vortex Rings," *Proc. Roy. Soc. Lond.*, 176, Part 2, 1885, pp. 725-780.

Johnson, G.M., "Researches on the Propagation and Decay of Vortex Rings," ARL 70-0093, Wright-Patterson AFB, OH, June 1970.

Kline, S.J. and McClintock, F.A., "Describing Uncertainties in Single-Sample Experiments," *Mechanical Engineering*, Vol. 75, 1953, pp. 3-8.

Kuethe, A.M. and Chow, C.Y., *Foundations of Aerodynamics*, Wiley 4th edition, 1986.

Lee, M., Reynolds, W.C., "Bifurcating and Blooming Jets," Symposium on Turbulent Shear Flows, 5th, Ithaca, NY, Aug. 7-9, 1985. University Park, PA, Pennsylvania State University, 1985, p. 1.7-1.12.

Leonard A., "Vortex Methods for Flow Simulation," *J. of Comp. Physics*, Vol. 37, 1980, pp. 289-335.

Leonard, A., "Computing Three-Dimensional Incompressible Flows with Vortex Elements," *Ann. Rev. Fluid Mech.*, Vol. 17, 1985, pp. 523-559.

Lockwood, R.M., "Pulse Reactor Lift-Propulsion System Development Program," Hiller Aircraft Company, Rept. No. ARD-308, March 1963.

Magarvey, R.H. and MacLatchy, C.S., "The Formation and Structure of Vortex Rings," *Canad. J. Physics*, Vol. 42, 1964(a), pp. 678-683.

Maxworthy, T., "The Structure and Stability of Vortex Rings," *J. Fluid Mech.*, Vol. 51, 1972, pp. 15-32.

Maxworthy, T., "Turbulent Vortex Rings," *J. Fluid Mech.*, Vol. 64, 1974, pp. 227-239.

Maxworthy, T., "Some Experimental Studies of Vortex Rings," *J. Fluid Mech.*, Vol. 81, 1977, pp. 465-495.

Parekh, D.E., Leonard, A., and Reynolds, W.C., "Bifurcating Jets at High Reynolds Numbers," Report No. TF-35, Thermosciences Division, Dept. of Mechanical Engineering, Stanford University, 1988.

Reynolds, W.C. and Bouchard, E.E., *Unsteady Turbulent Shear Flows*, "The Effect of Forcing on the Mixing-Layer Region of a Round Jet," Springer-Verlag, New York, 1981, pp. 402-411.

Rosenhead, L., "The Formation of Vortices from a Surface of Discontinuity," *Proc. Roy. Soc. Series A*, Vol. 134, 1931, pp. 170-192.

Sallet, D.W. and Widmayer, R.E., "An Experimental Investigation of Laminar and Turbulent Vortex Rings in Air," *Z. Flugwiss.*, Vol. 22, 1974, pp. 207-215.

Sarohia, V. and Bernal, L.P., "Entrainment and Mixing in Pulsatile Jets," Proceedings of the 3rd Symp. Turbulent Shear Flow, 1981, pp. 11.30-11.35.

Sarpkaya, T., "Computational Methods with Vortices- The 1988 Freeman Scholar Lecture," *J. Fluid Engineering*, Vol. 111, March, 1989, pp. 5-52.

Thomson, J.J., A Treatise on the Motion of Vortex Rings, Macmillan, London, 1883.

Ting, L. and Tung, C., "Motion and Decay of a Vortex in a Non uniform Stream," *Physics of Fluids*, Vol. 8, No. 6, 1965, pp. 1039-1051.

Vandsburger, U., Lewis, G., Seitzman, J.M., and Allen, M.G., "Flame-Flow Structure in an Acoustically Driven Jet Flame," Western States Section/The Combustion Institute Fall Meeting, University of Arizona, Paper 86-19, 1986.

Whitehead, K.D., "The Generation and Development of a Viscous Vortex Ring," Georgia Institute of Technology, School of Aerospace Engineering, Rep. 68-4, 1968.

Wu, J.M., Vakili, A.D., and Yu, F.M., "Investigation of Interacting Flow of Nonsymmetric Jets in Cross-Flow," *AIAA J.*, Vol. 26, 1988, pp. 940-947.

Table 1
Quantitative data from hot-film measurement

Z	$3d_j$	$7d_j$	$10d_j$
Ring radius R, cm	1.080	1.250	1.397
Translational velocity $U_T, \text{cm/sec}$	9.635	9.162	8.471
Radius ratio a/R	0.294	0.279	0.268
Measured circulation $\Gamma_m, \text{cm}^2/\text{sec}$	38.526	35.183	33.631
Core circulation $\Gamma_c, \text{cm}^2/\text{sec}$	25.896	23.326	21.615
Ideal circulation $\Gamma_i, \text{cm}^2/\text{sec}$	39.879	39.879	39.879
Mean pulsating velocity $\bar{u}, \text{cm/sec}$	12.630	12.630	12.630
Reynolds number $Re = \frac{\Gamma_i}{\nu}$	3970	3970	3970
Tilting angle	2.6°	3.2°	3.3°
$\ln(\frac{8R}{a}) - \frac{1}{4}$ in inviscid equation	3.054	3.106	3.146
Non-dimensional velocity \tilde{U}	3.610	4.411	4.919
X-coordinate of ring center	$0.40d_j$	$1.24d_j$	$1.78d_j$

Table 2
Comparative data on vortex ring formation

	Ring formation distance	Re_{ex}	Medium
Whitehead (1968)	$2.0d_j$	533	Computation
Sallet et al. (1974)	$2.5d_j$	8010 – 12250	Experiment in air
This study	$3.0d_j$	800	Experiment in water

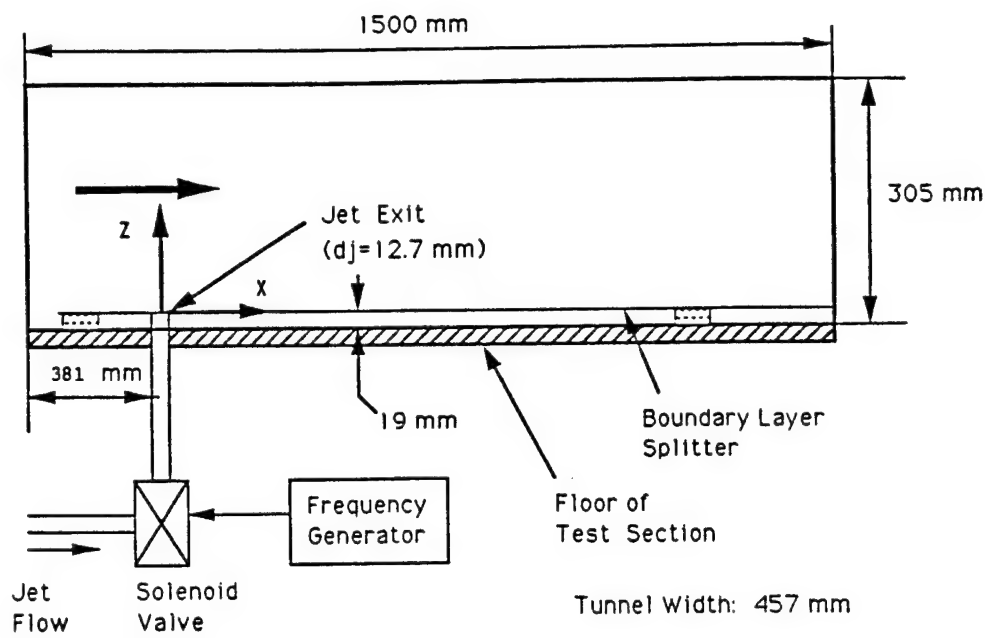


Figure 1. Experimental setup of water tunnel for continuous pulsation.

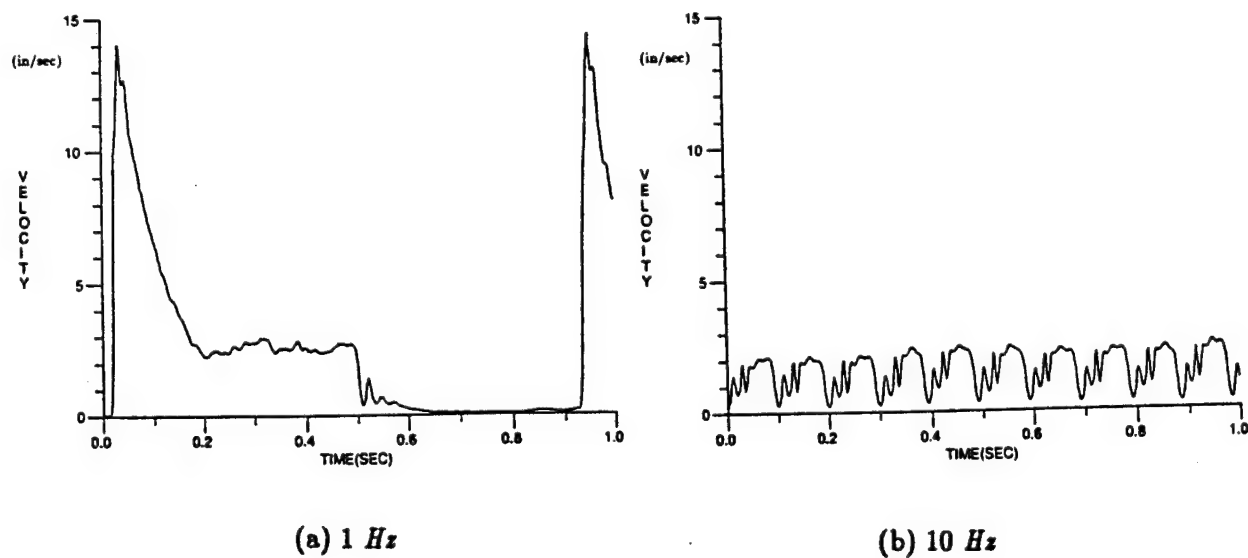


Figure 2. Typical pulsation profiles at the exit.

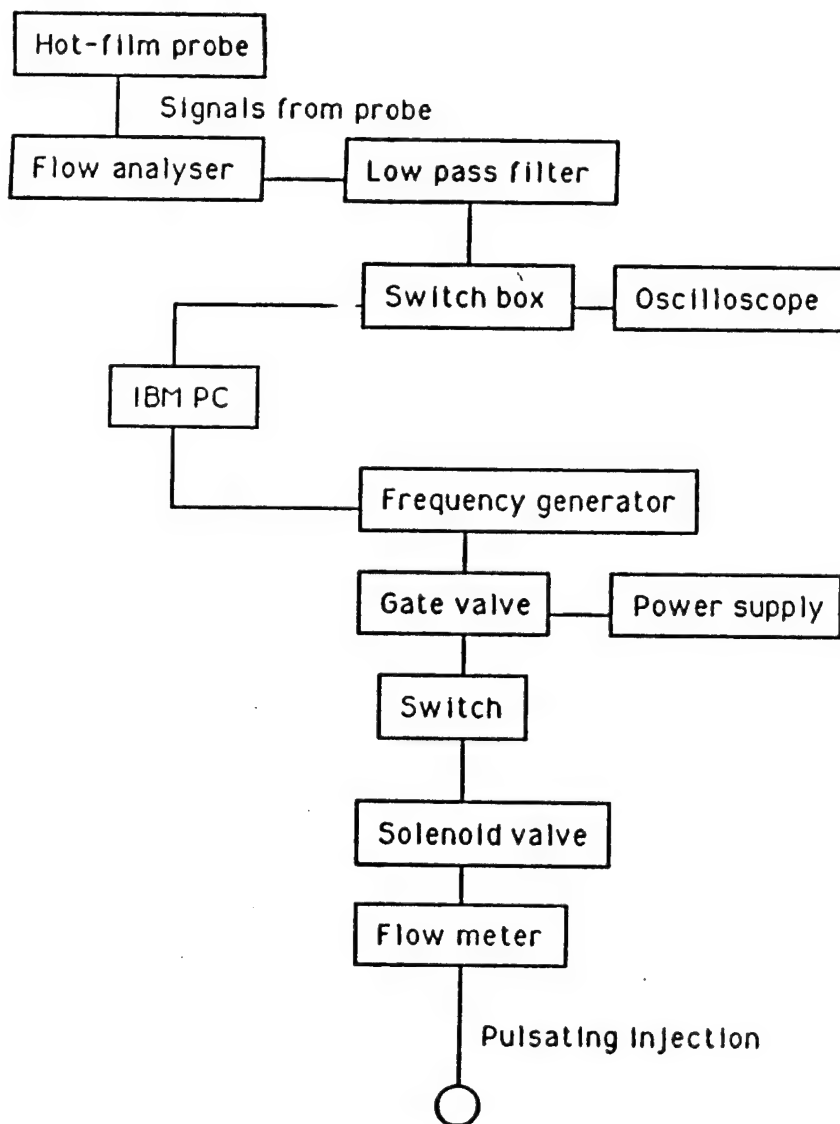
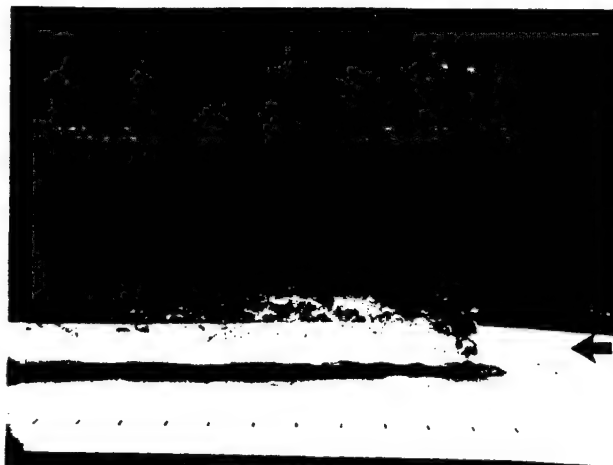


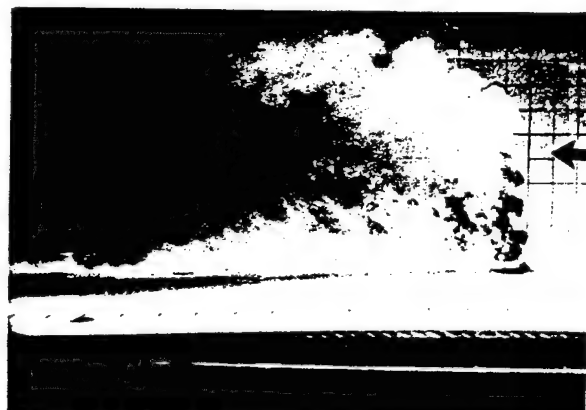
Figure 3. Schematic diagram for thermal anemometer and data acquisition system



(a) Pulsed at 1 Hz



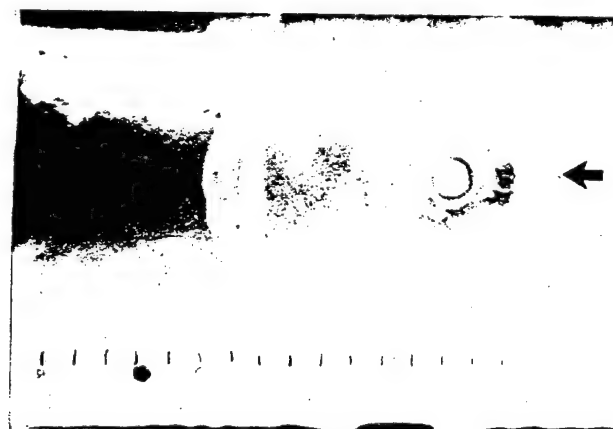
(b) Pulsed at 2 Hz



(c) Pulsed at 10 Hz



(d) Steady jet



(e) Top view of a ring at 1 Hz

Figure 4.

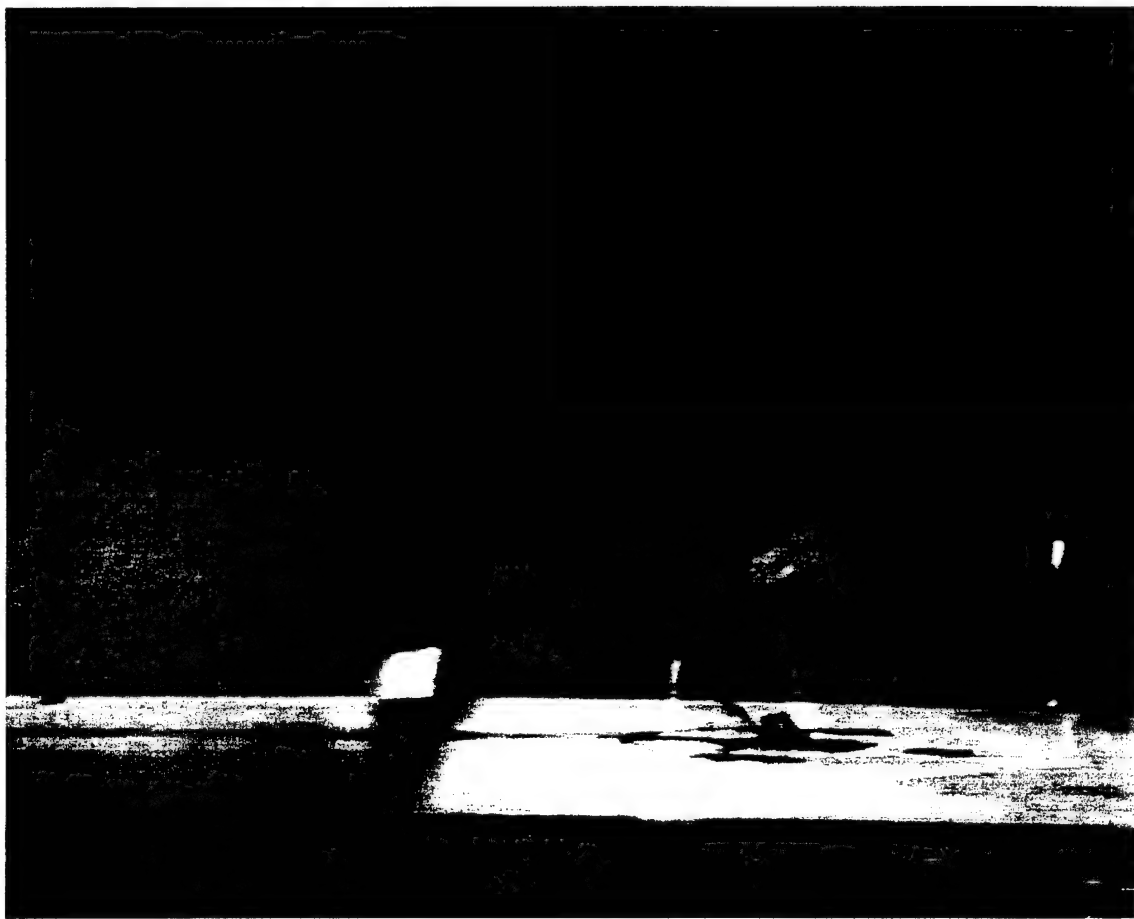


Figure 4. Typical photographs of vortex rings in cross-flow for various pulsation and flow conditions for $\bar{U}_j/U_\infty = 1.5$, $Re_d = 1870$

- (a) Pulsed at 1 Hz, (b) Pulsed at 2 Hz, (c) Pulsed at 10 Hz, (d) Steady Jet,
- (e) Top view of a ring, jet is pulsed at 1 Hz.
- (f) A single ring moving into the cross-flow, note the upstream motion caused by the tilting process

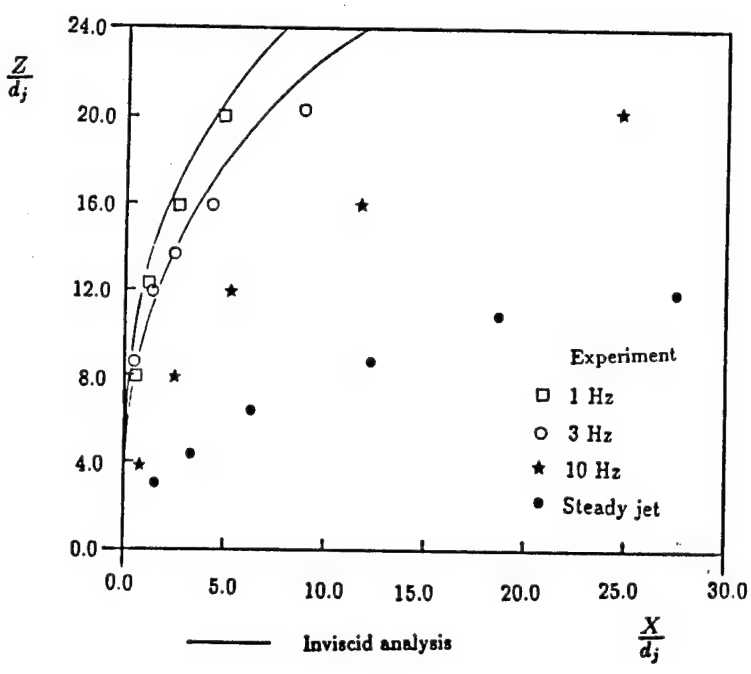
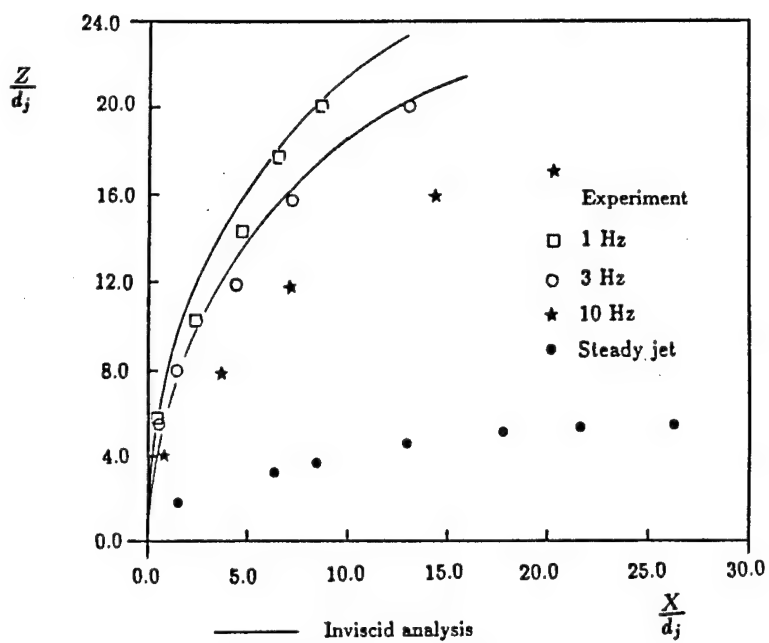
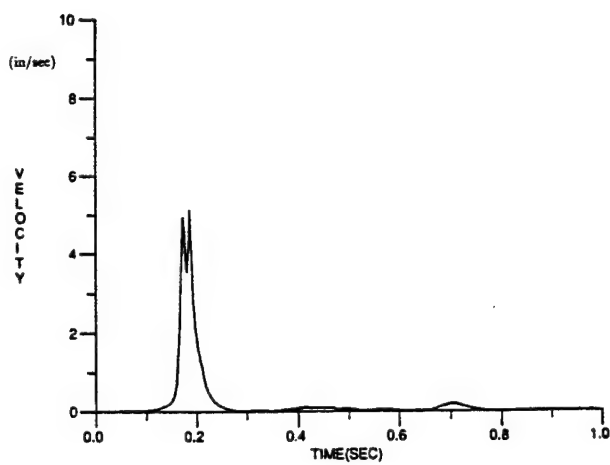
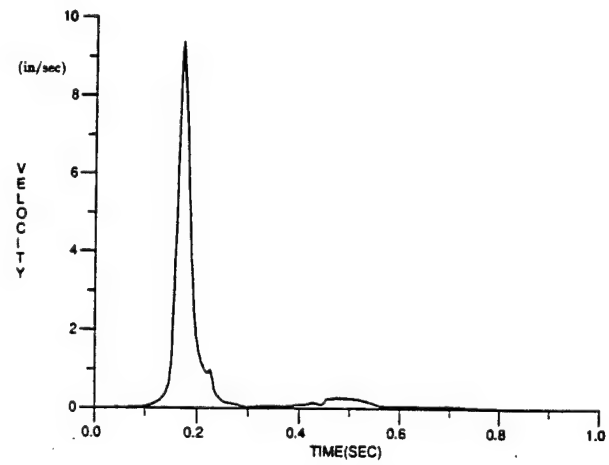


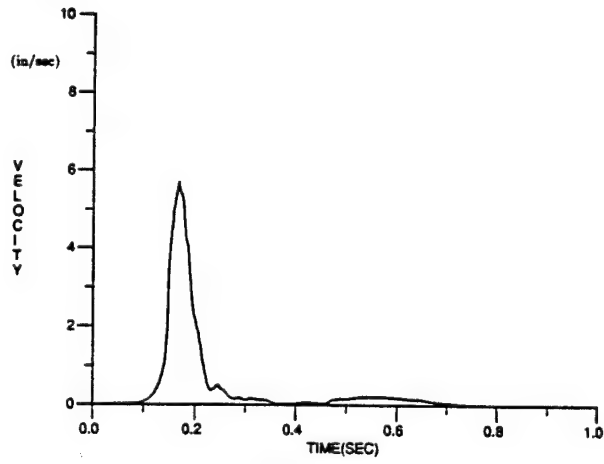
Figure 5. Penetration Trajectories of vortex rings in the cross-flow for various pulsating frequencies



(a) At the core center

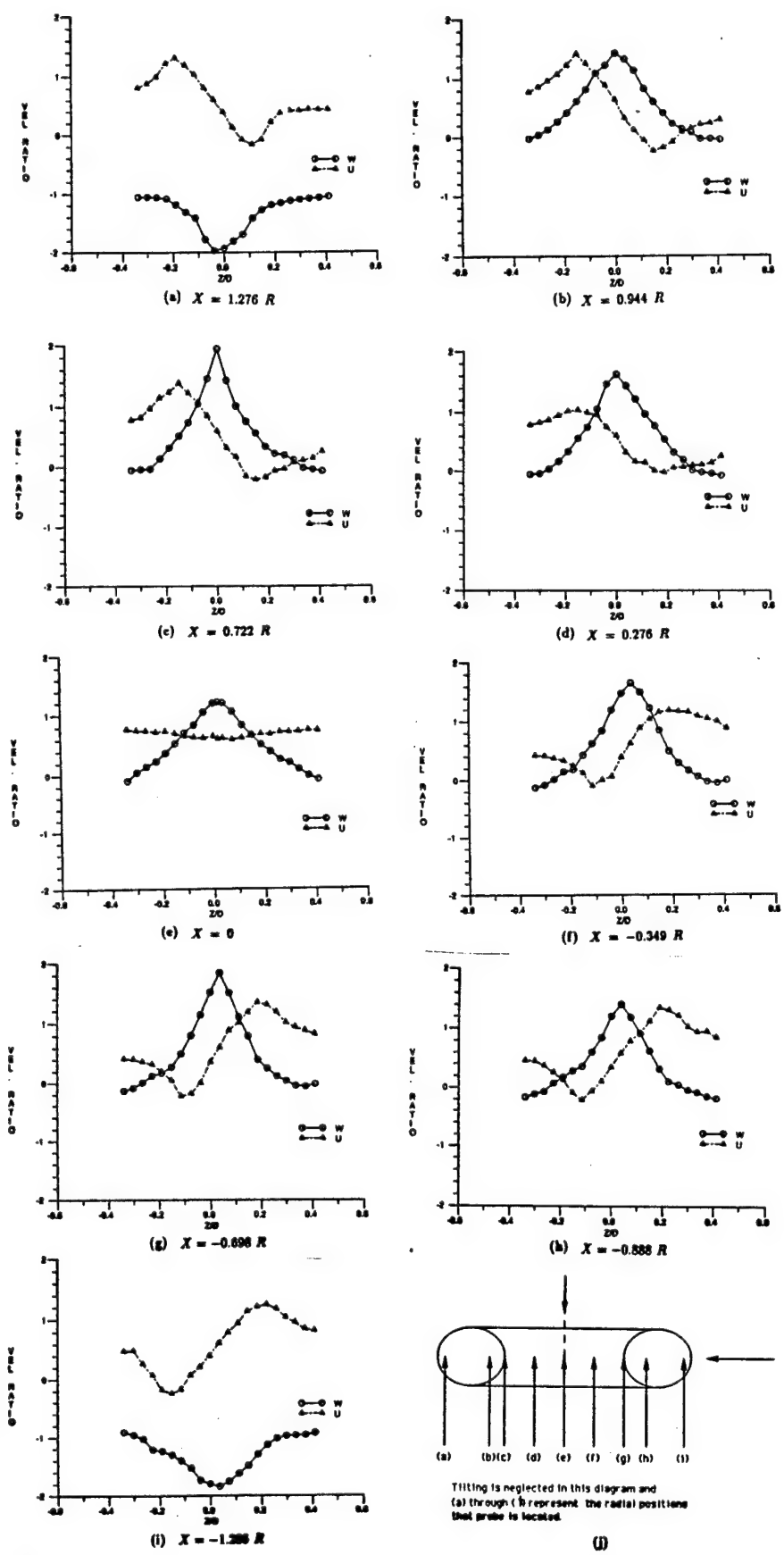


(b) At the inner edge of core



(c) At the ring center

Figure 6. Some typical velocity traces at $Z = 3d_j$



Tilting is neglected in this diagram
(a) through (i) represent the radial positions
that probe is located.

(j)

Figure 7. Typical velocity flow-field within a ring at $Z = 3d$,
(a) through (i) are schematically explained in Figure 4.7(j)

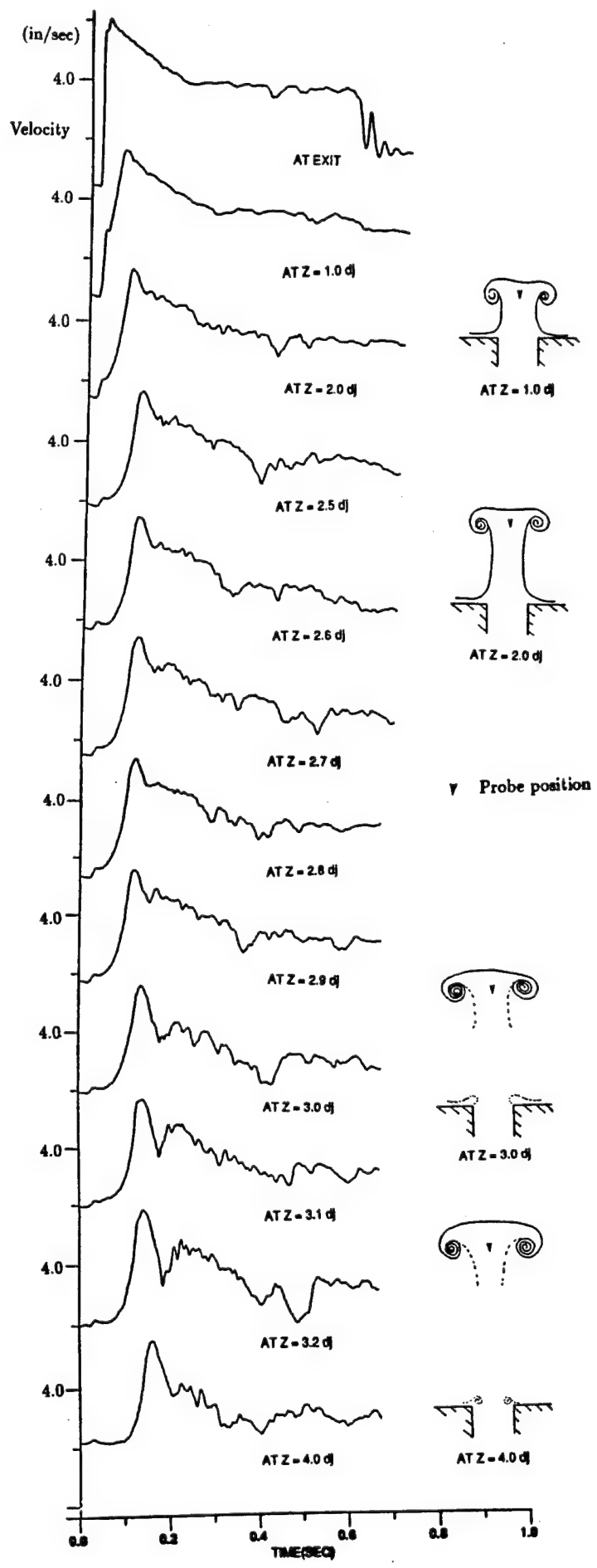


Figure 8. Sequence of traces showing fully-formed vortex ring

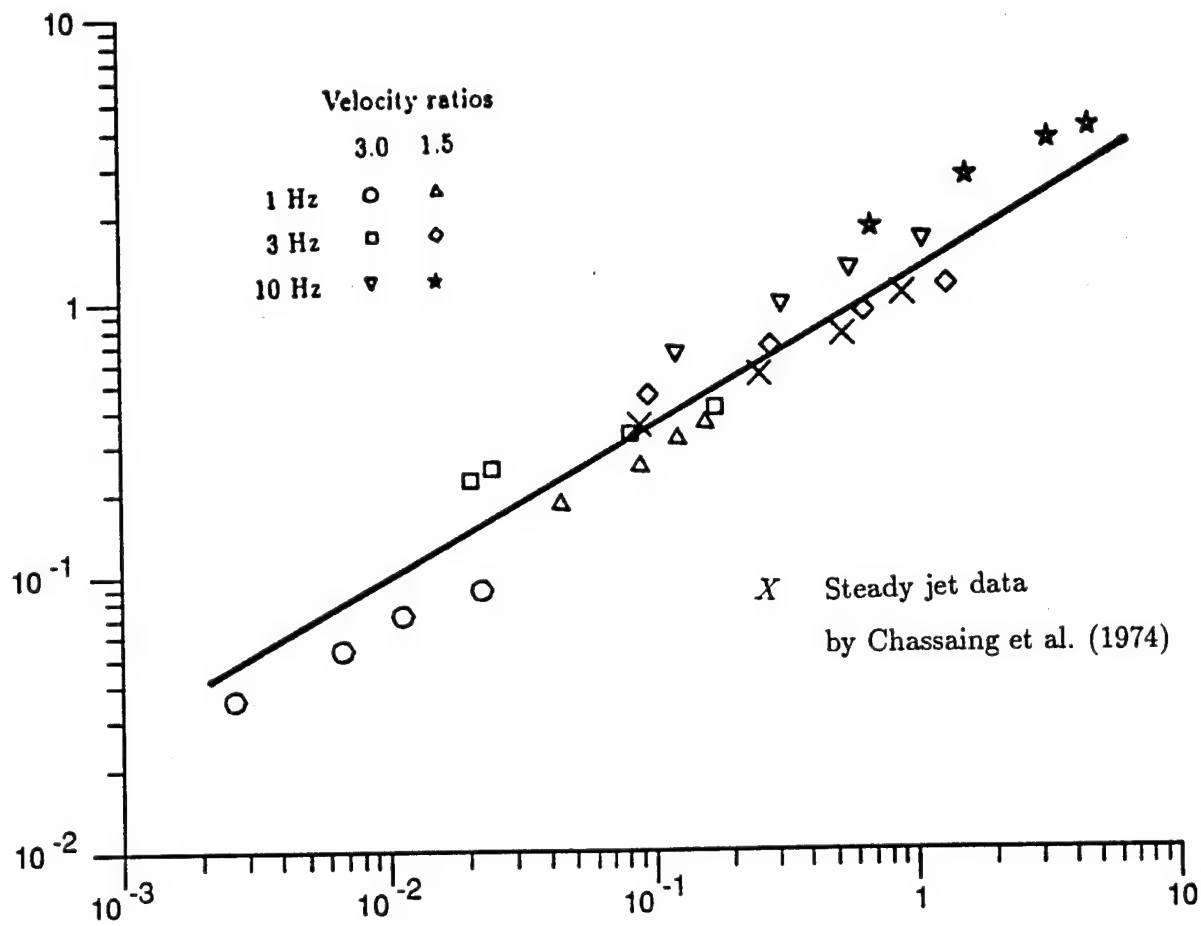


Figure 9. Collapsed trajectory for pulsating jet

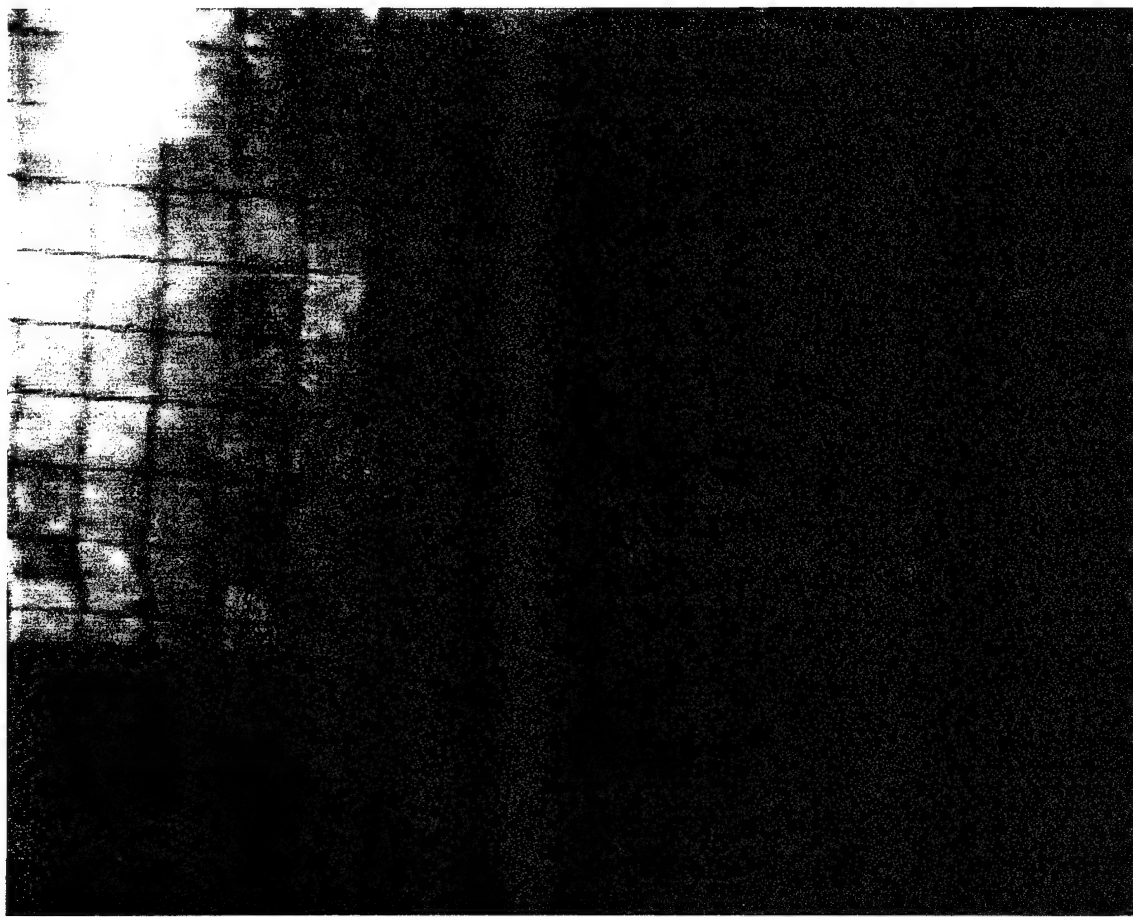


Figure 10. Blooming jet observed without any active control of the exit geometry.

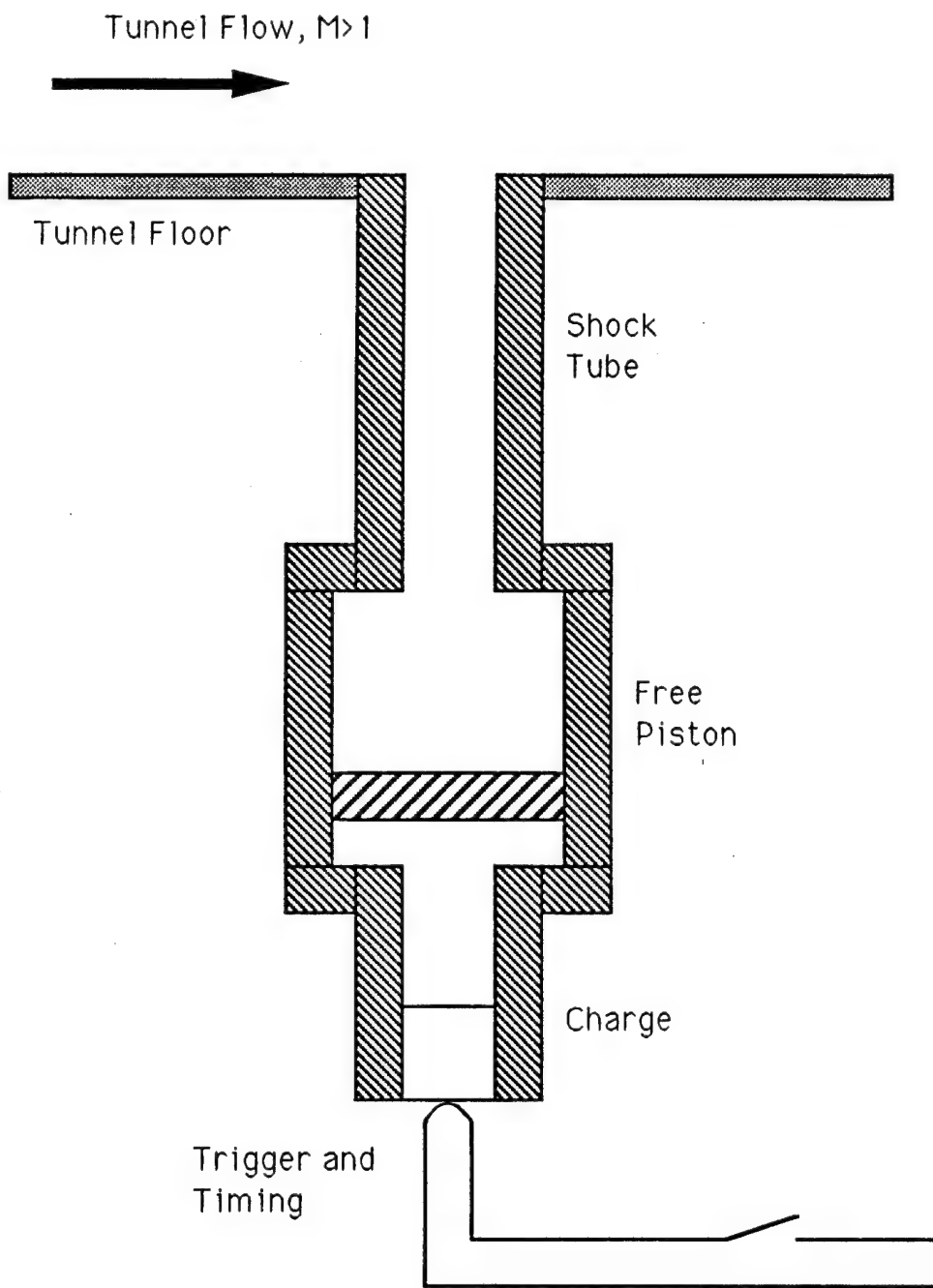


Figure 11. Schematic of the shock tube used to create a pulsed flow into a high speed cross-flow

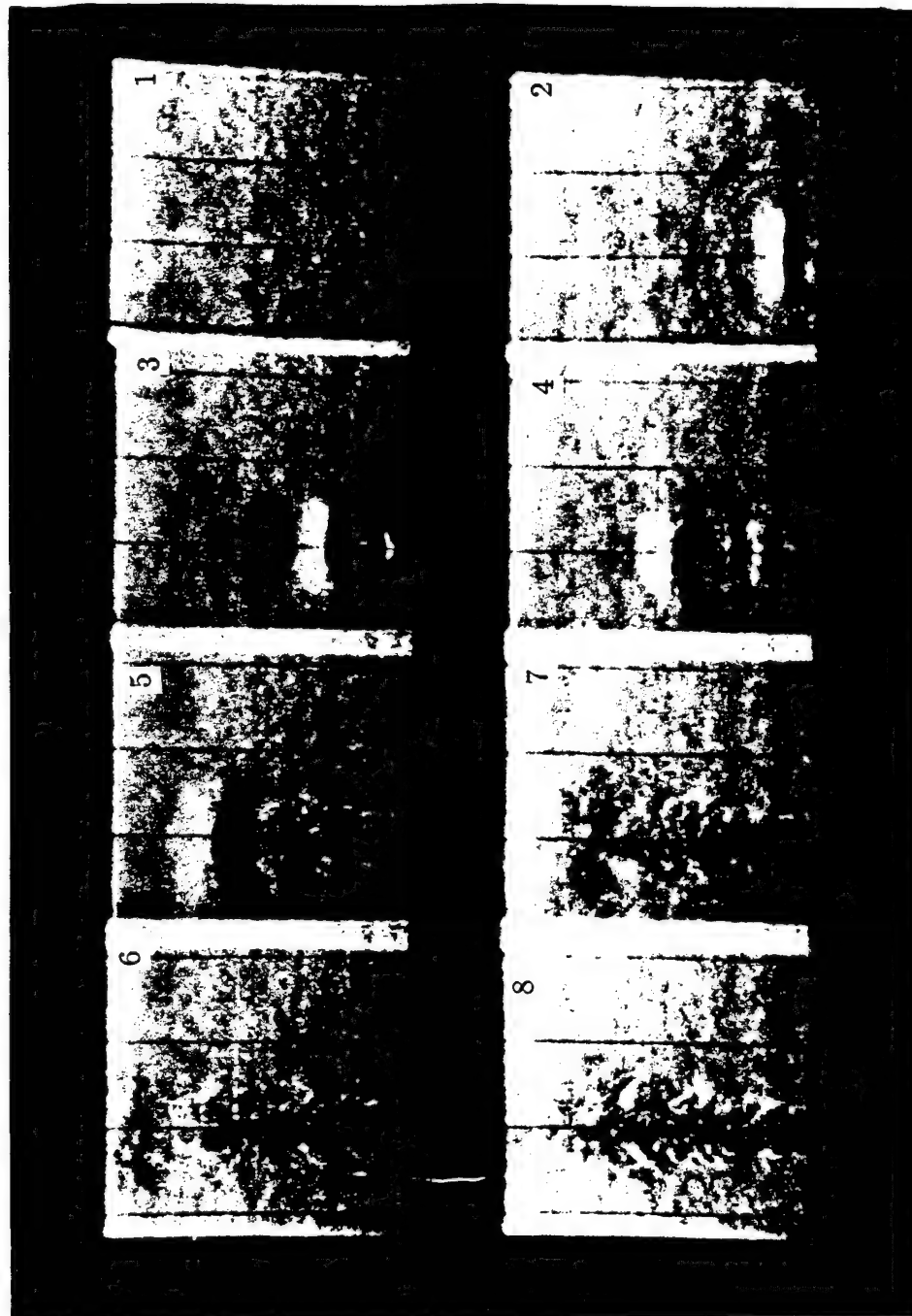


Figure 12. Sequence of a pulsed jet comming out of the shock tube into still air. Each frame is taken in 20 microseconds with 100 microseconds between sequential frames.

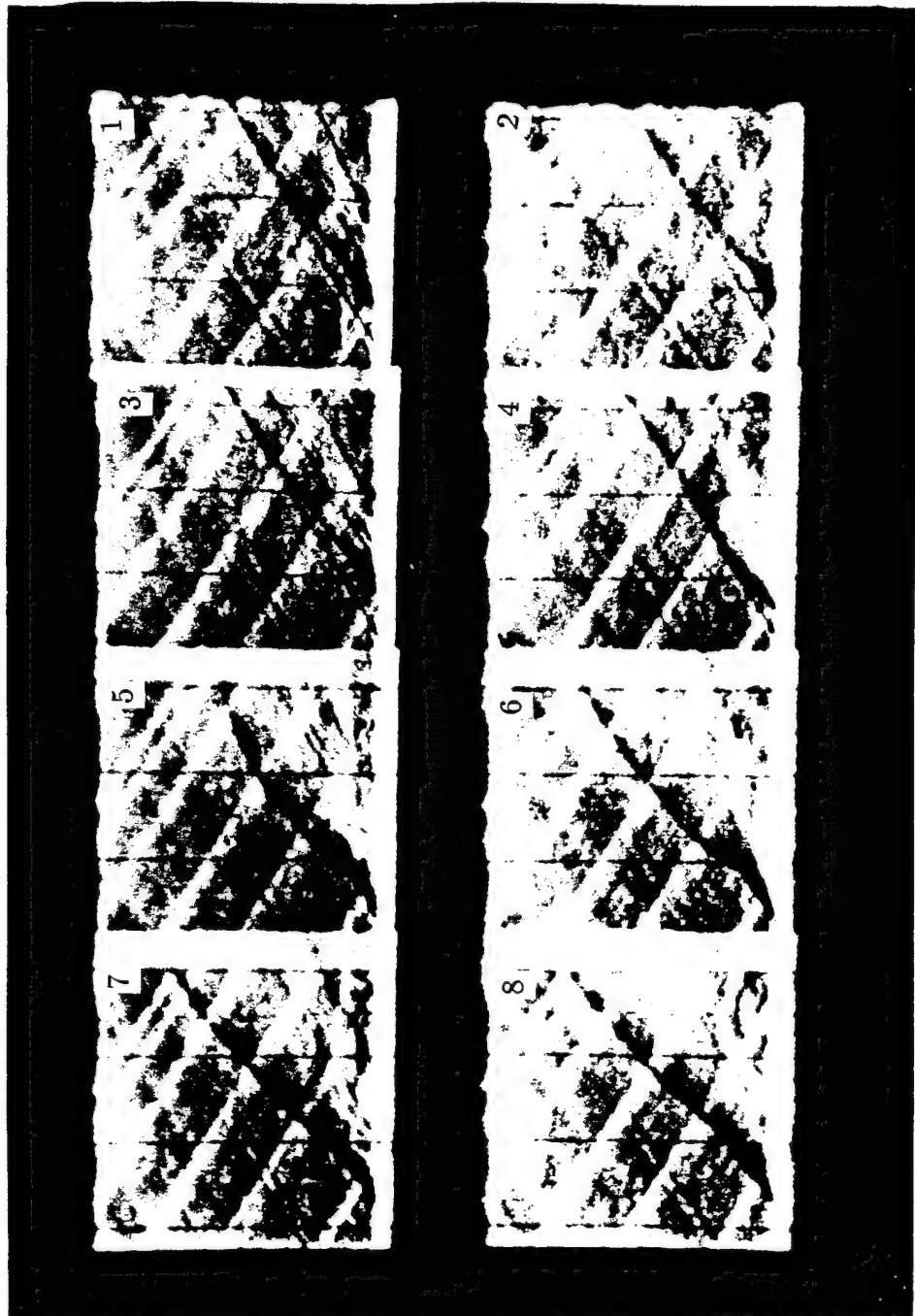


Figure 13. Sequence of a pulsed jet coming out of the shock tube into a 1.80 Mach cross flow of air. Initial delay time of 550 microsecond. Each frame is taken in 20 microseconds with 100 microseconds between sequential frames.

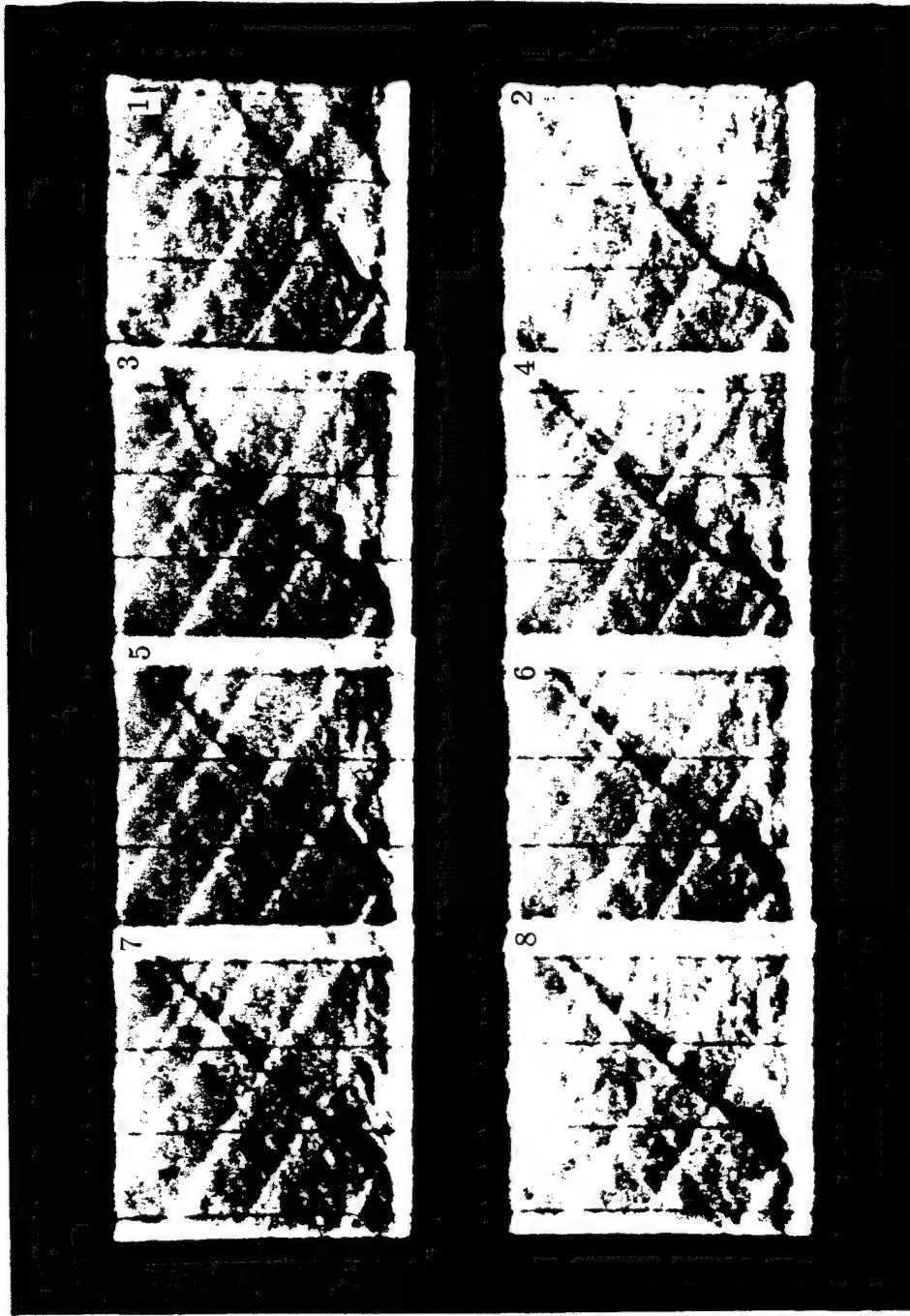


Figure 14. Sequence of a pulsed jet coming out of the shock tube into a 1.80 Mach cross flow of air. Initial delay time of 650 microsecond. Each frame is taken in 20 microseconds with 100 microseconds between sequential frames.

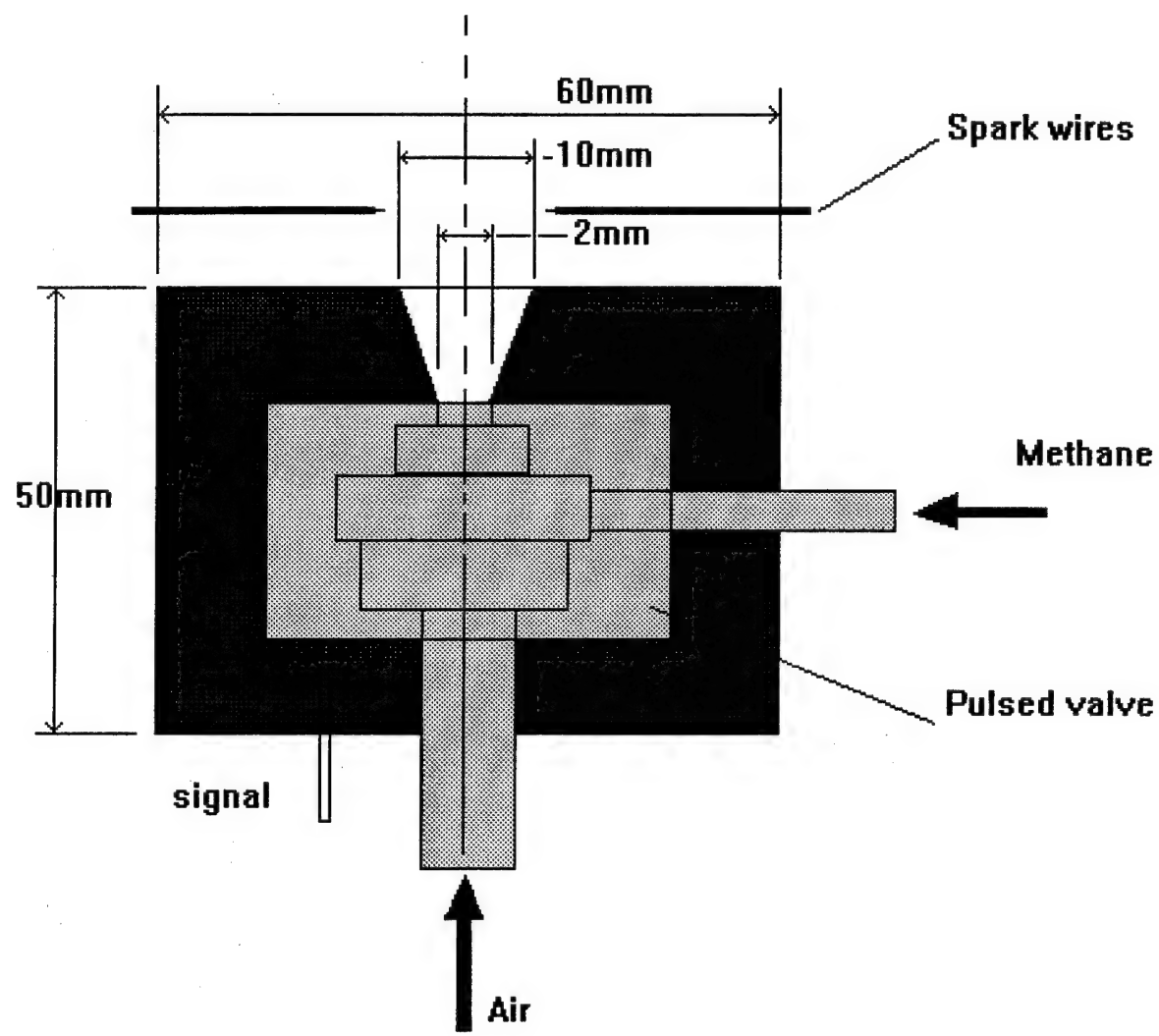


Figure 15. Schematic of the quartz pulsed valve and the set-up for combustion of methane in air.

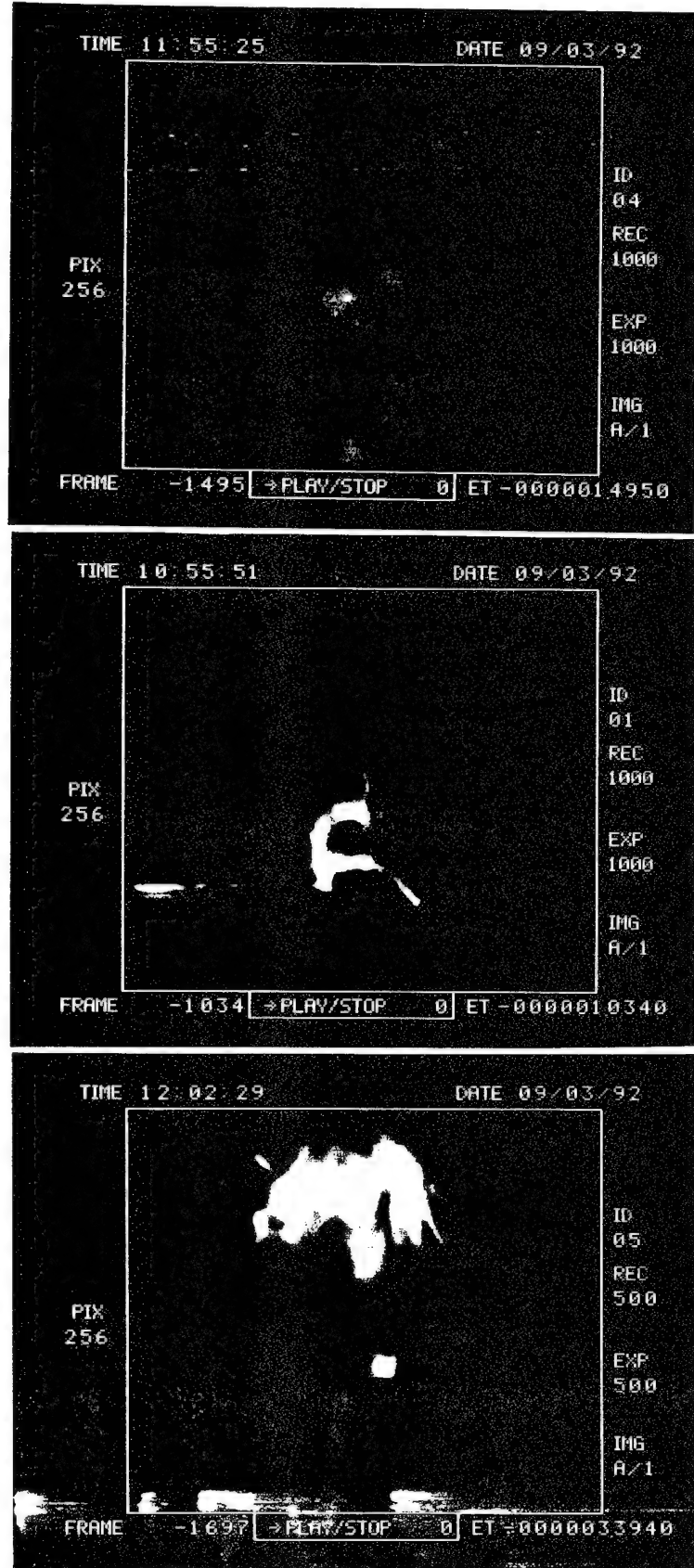
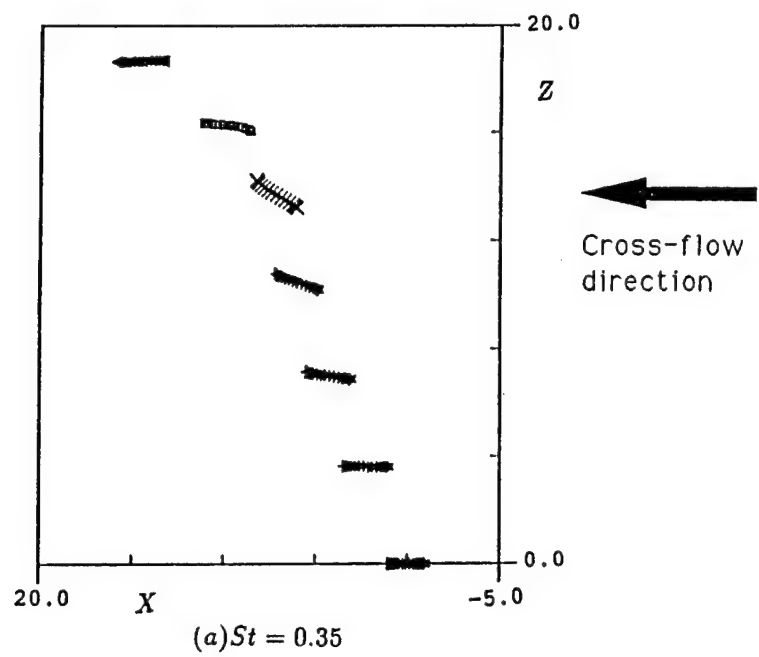
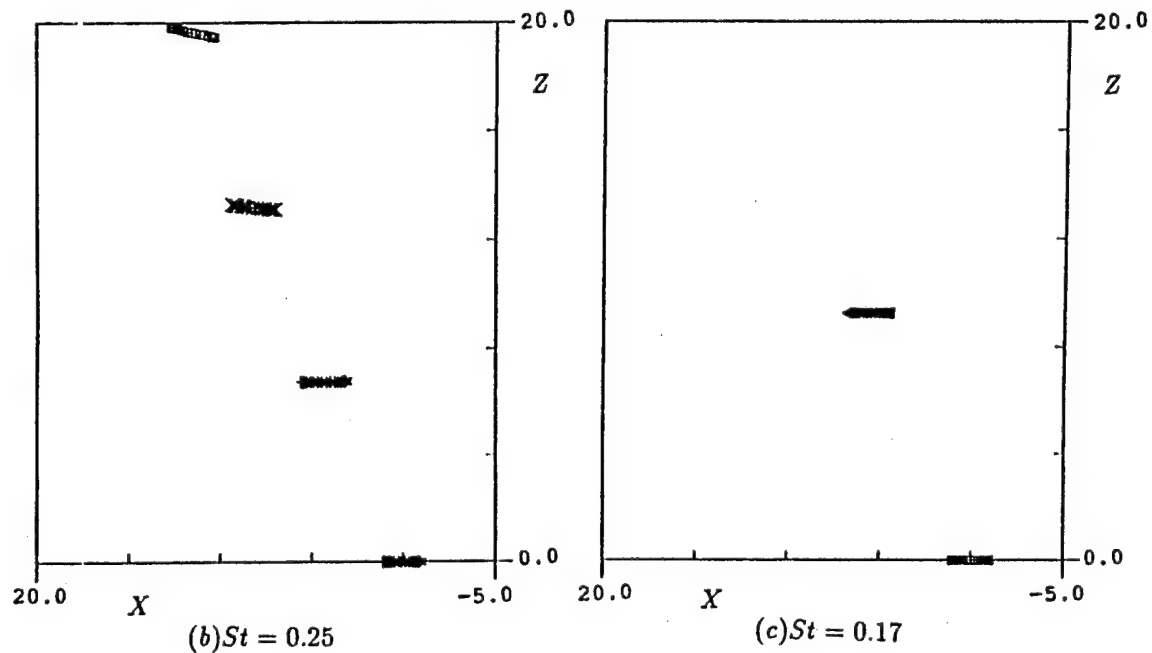


Figure 16. Combusting images of a pulsed fuel jet into ambient air at 20 Hz. Burning vortex rings are apparent.



(a) $St = 0.35$



(b) $St = 0.25$

(c) $St = 0.17$

Figure 17. Effect of frequency on motion and trajectory at $U_\infty = 0.125, \Gamma = 1.0$

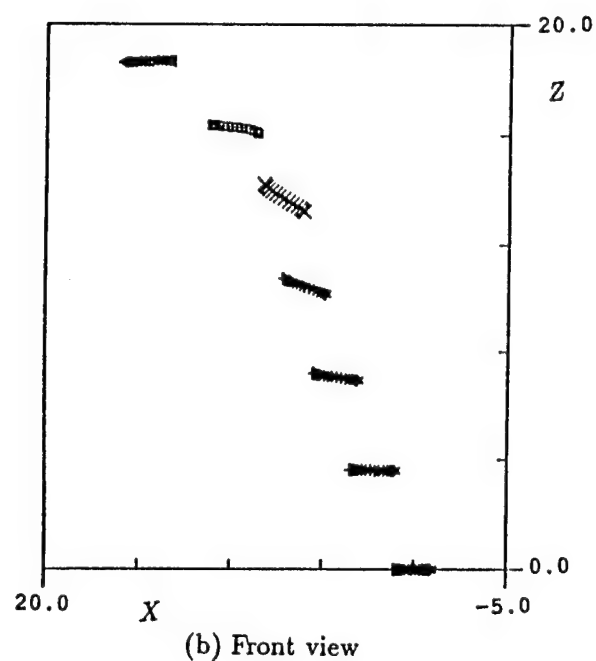
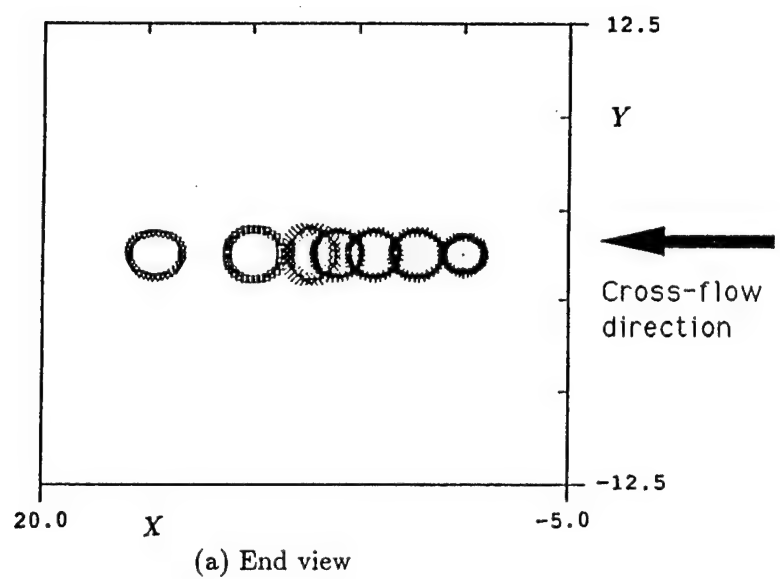
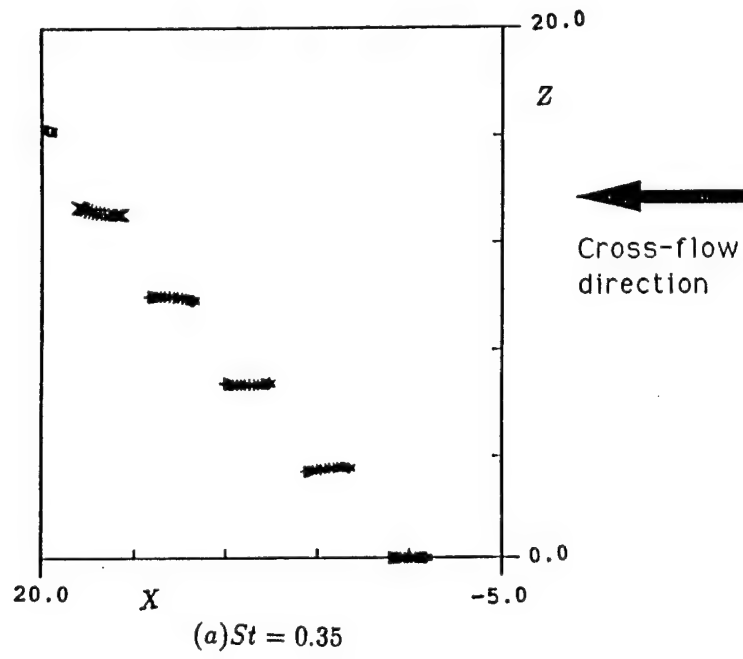


Figure 18. Typical vortex ring evolution at $St = 0.35$, $\Gamma = 1.0$, $U_\infty = 0.125$



(a) $St = 0.35$

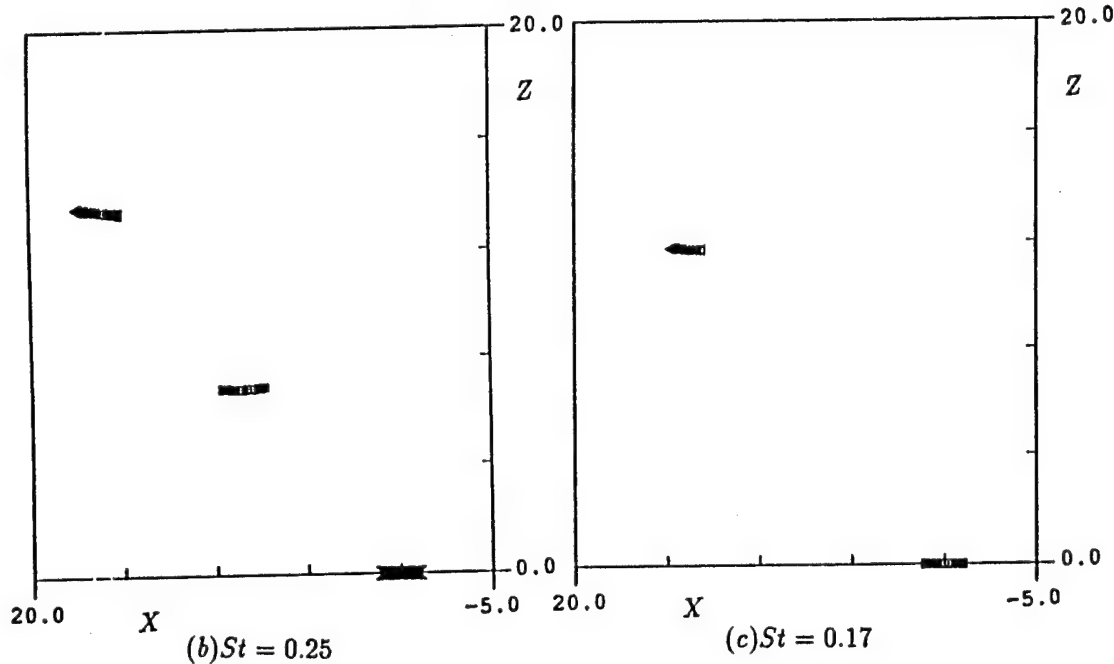
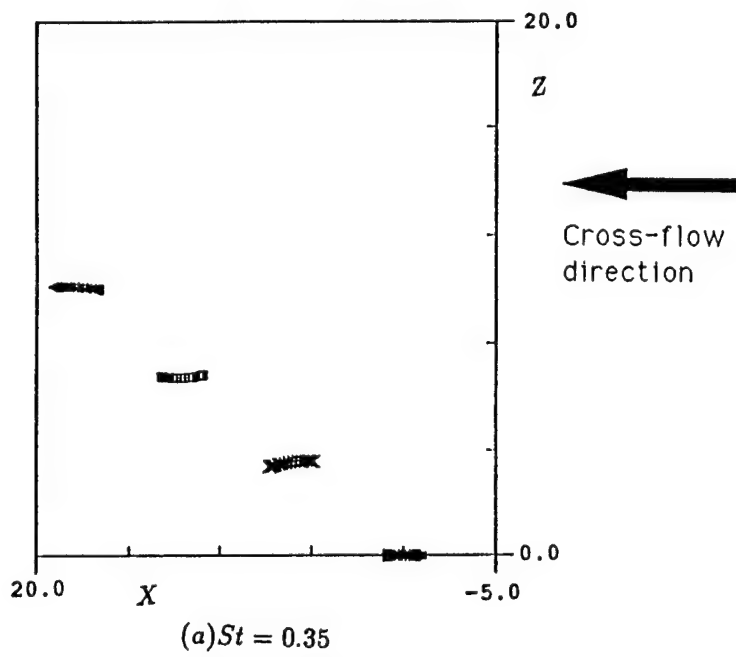


Figure 19. Effect of frequency on motion and trajectory at $U_\infty = 0.250, \Gamma = 1.0$



(a) $St = 0.35$

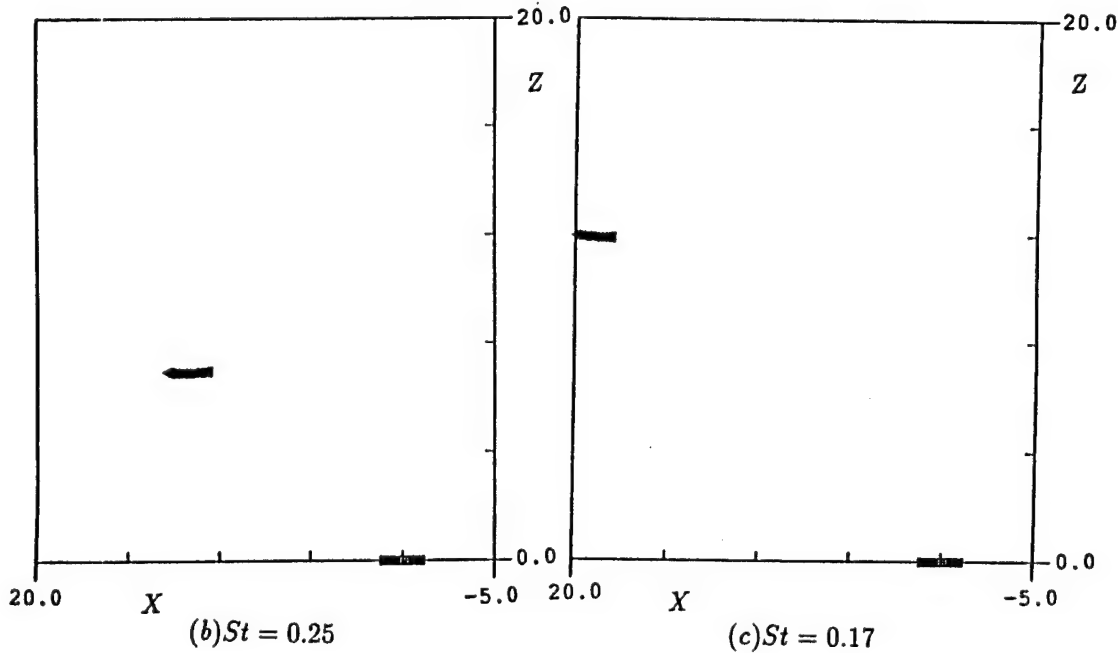
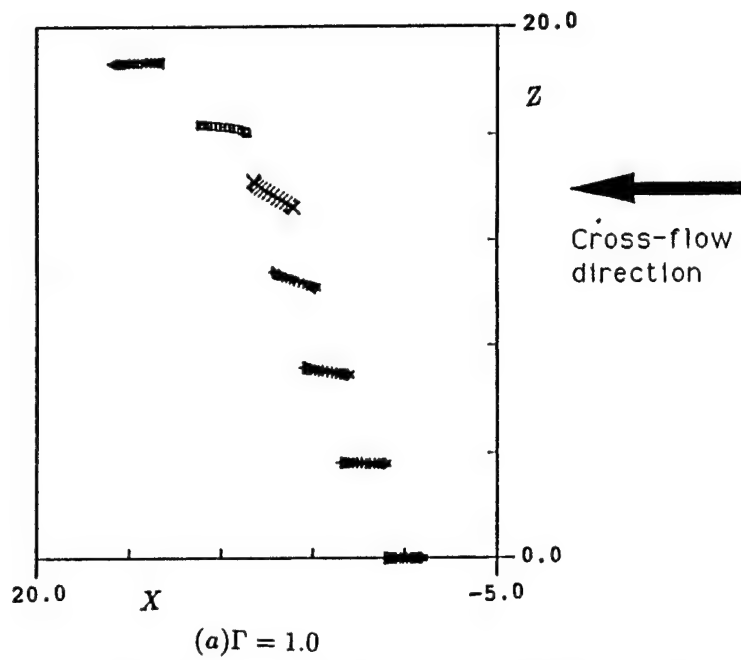
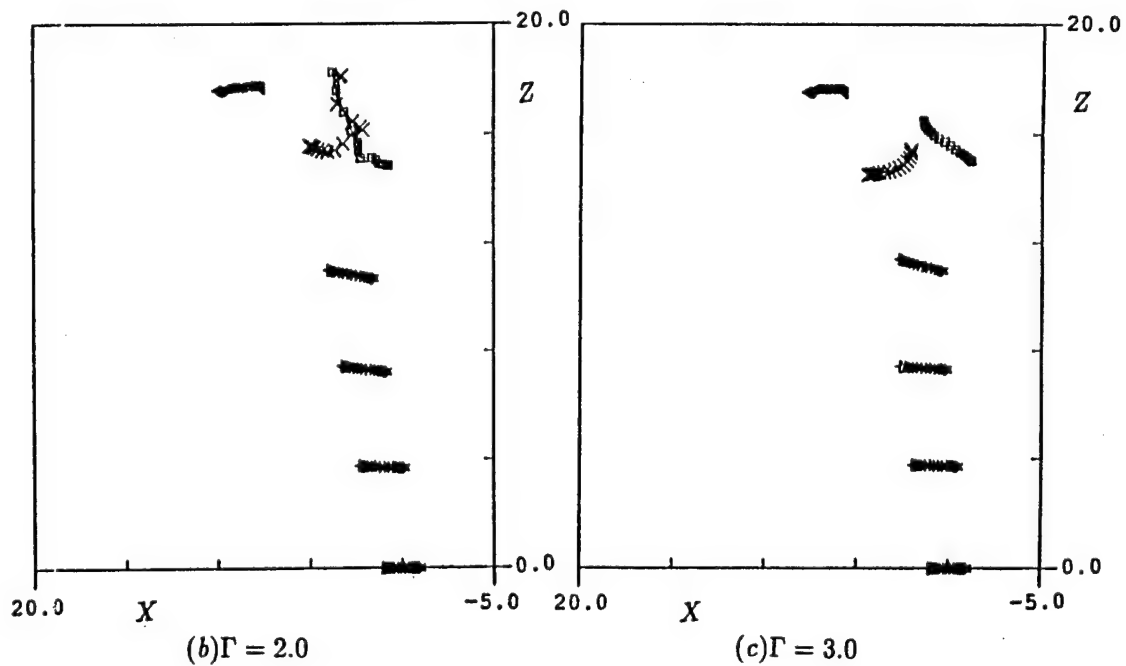


Figure 20. Effect of frequency on motion and trajectory at $U_\infty = 0.350, \Gamma = 1.0$



(a) $\Gamma = 1.0$



(c) $\Gamma = 3.0$

Figure 21. Effect of circulation on motion and trajectory at $St = 0.35, U_\infty = 0.125$

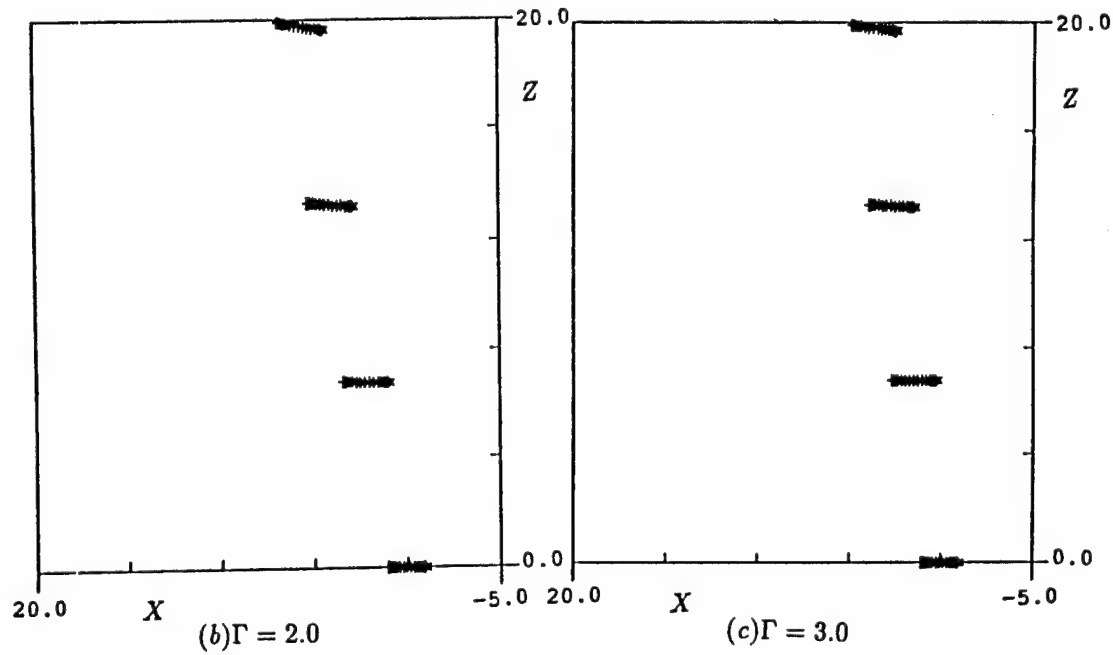
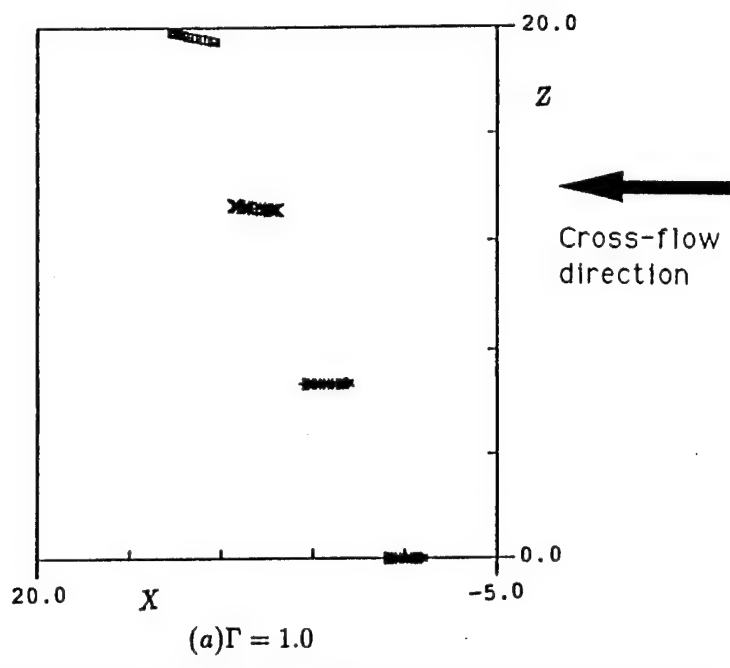
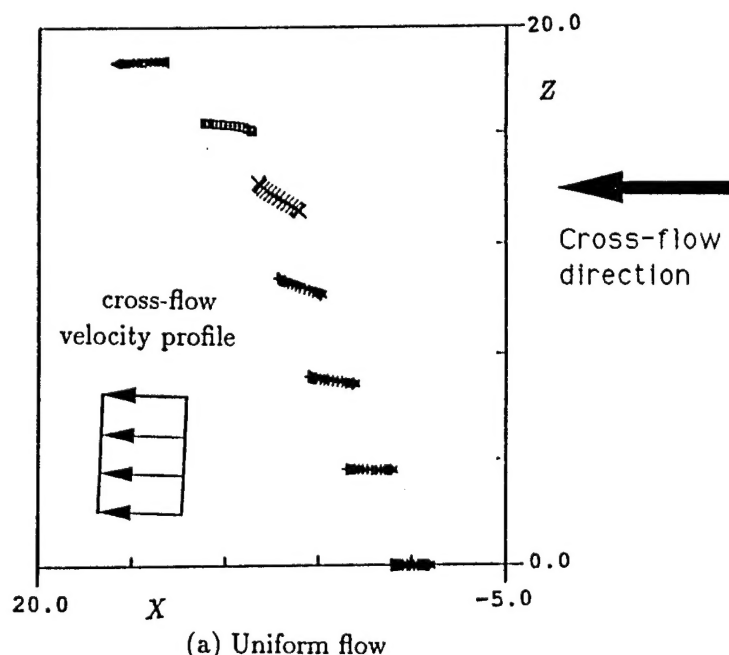


Figure 22. Effect of circulation on motion and trajectory at $St = 0.25, U_\infty = 0.125$



(a) Uniform flow

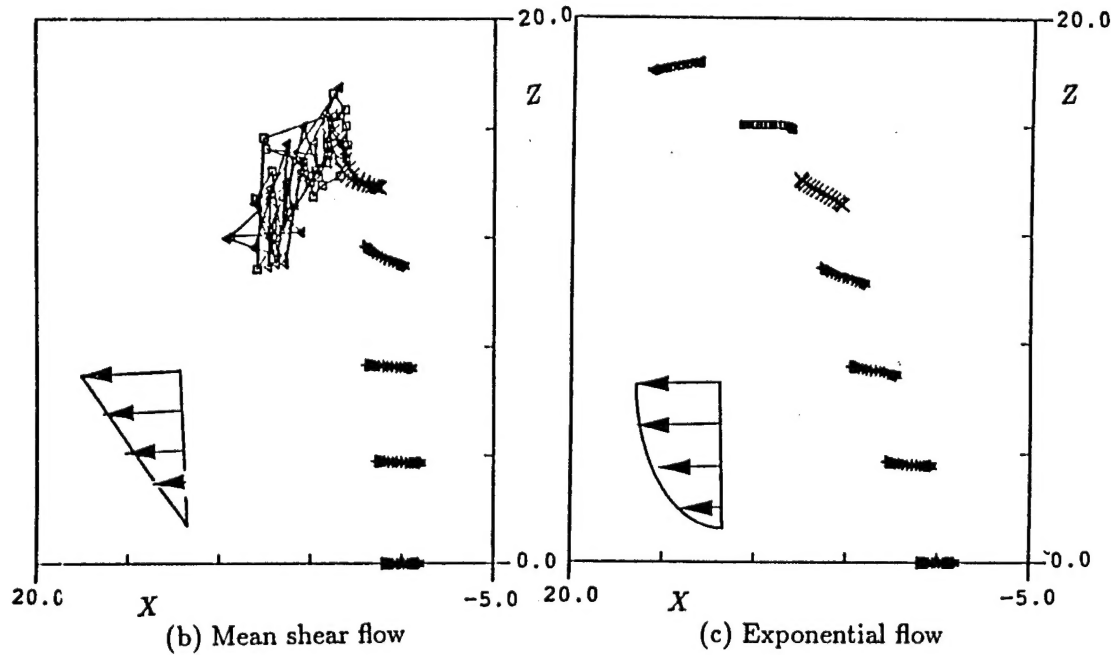
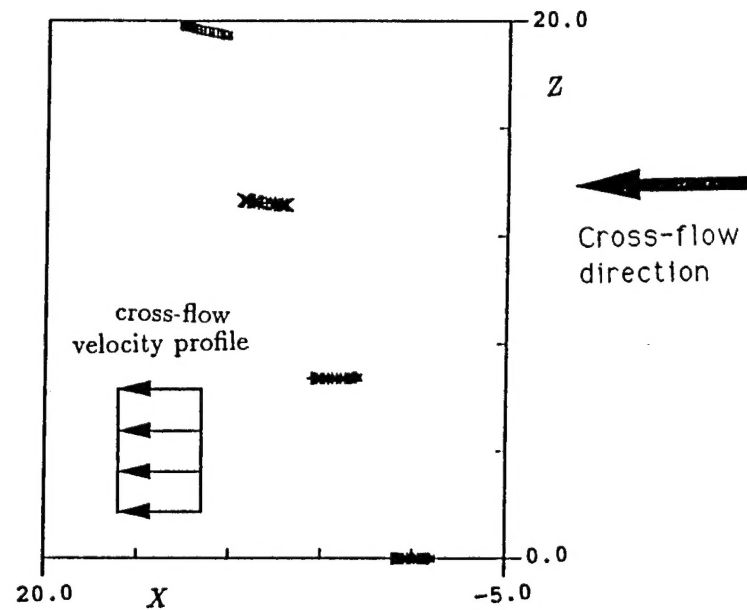


Figure 23. Effect of cross-flow on motion and trajectory at $St = 0.35, \Gamma = 1.0$



(a) Uniform flow

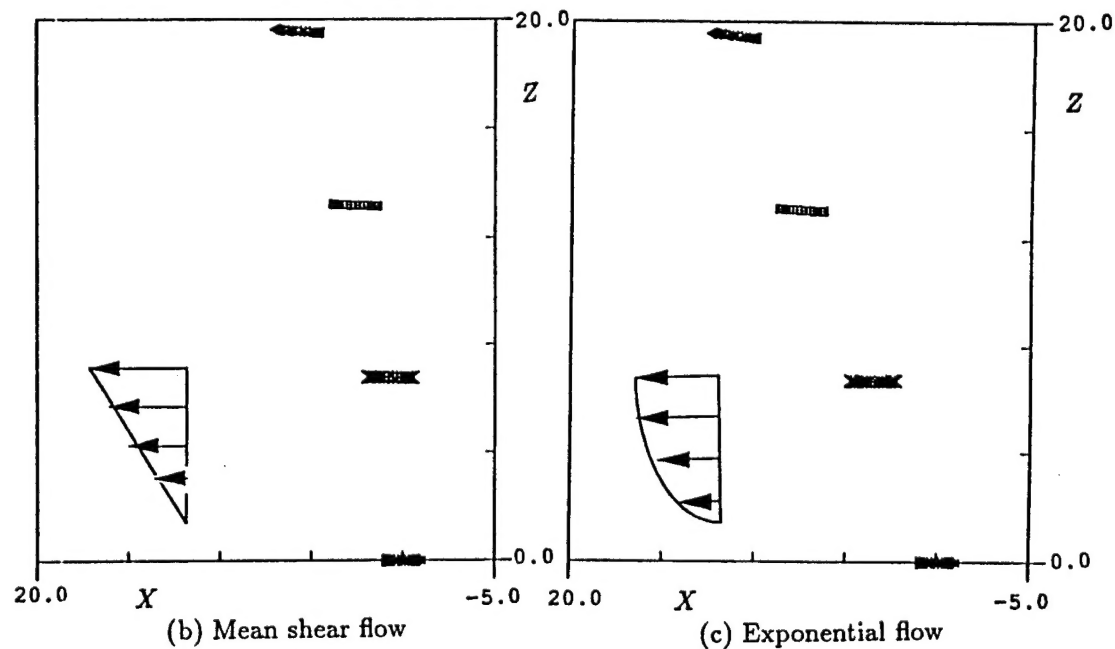
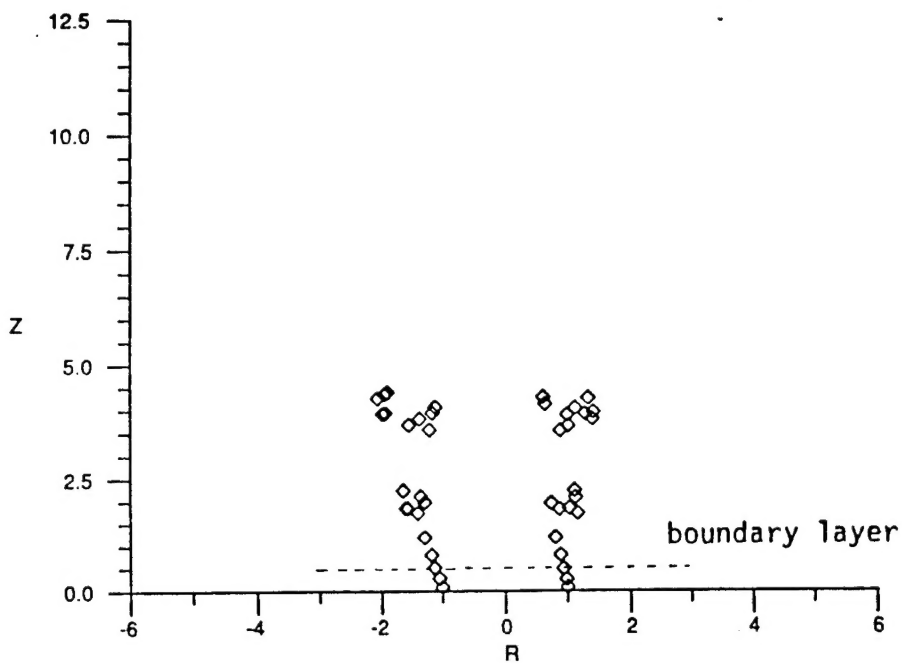
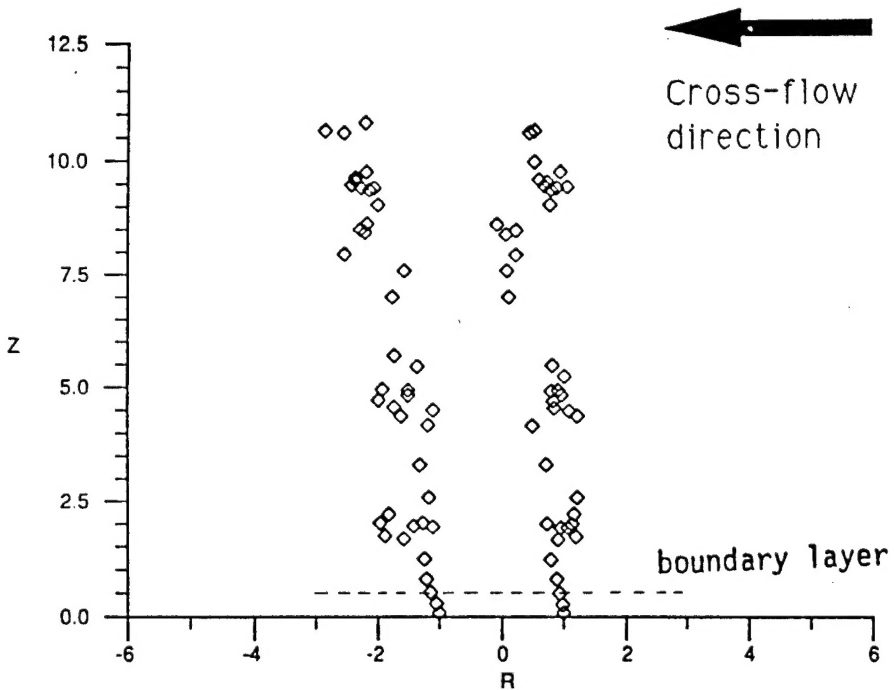


Figure 24. Effect of cross-flow on motion and trajectory at $St = 0.25, \Gamma = 1.0$

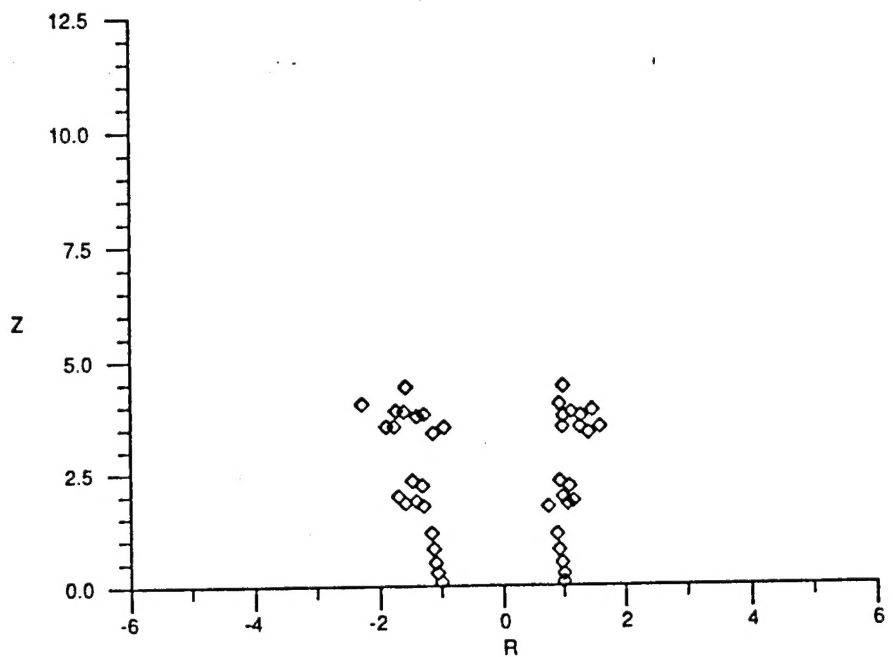


(a) $t = 10.0$

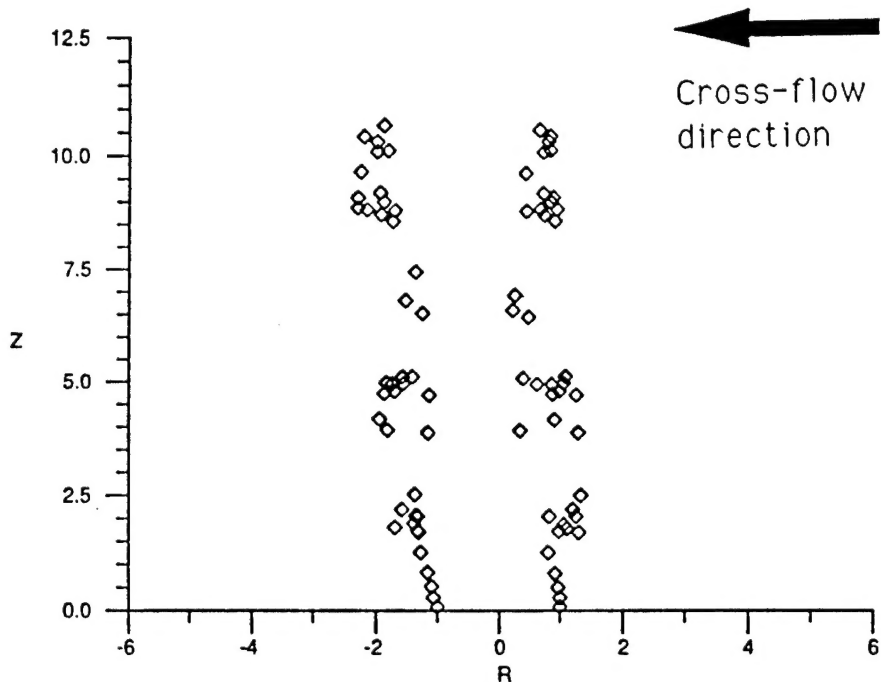


(b) $t = 20.0$

Figure 25. Time evolution of jet pulses, issued in a uniform cross-flow, and the formation of vortex rings.



(a) $t = 10.0$



(b) $t = 20.0$

Figure 26. Time evolution of jet pulses, issued in a shear cross-flow, and the formation of vortex rings.